universität wien

MASTERARBEIT / MASTER'S THESIS

Titel der Masterarbeit / Title of the Master's Thesis

„A Charged Particle Veto Detection System for Kaonic Deuterium Measurements at DAΦNE“

verfasst von / submitted by

Marlene Tüchler BSc

angestrebter akademischer Grad / in partial fulfilment of the requirements for the degree of

Master of Science (MSc)

Wien, 2019 / Vienna, 2019

Studienkennzahl lt. Studienblatt / degree programme code as it appears on the student record sheet:	A 066 876
Studienrichtung lt. Studienblatt / degree programme as it appears on the student record sheet:	Masterstudium Physik
Betreut von / Supervisor:	Priv.-Doz. Dr. Johann Zmeskal

Abstract

In the non-perturbative, low-energetic regime of QCD, the interaction between antikaons and nucleons close to threshold still poses many unresolved questions and is thus the subject of extensive research. The study of the $\overline{\mathrm{K}}\mathrm{N}$ interaction allows to gain insight in the complex processes of chiral symmetry breaking, leading to a better understanding of fundamental concepts in hadron physics like the origin of the hadron masses.
X-ray spectroscopy of kaonic atoms provides a versatile tool to study the strong interaction at low relative energies via a direct observation of its influence on the ground state of kaonic atoms. The SIDDHARTA-2 experiment, currently under construction at the DAΦNE collider complex in Frascati, Italy, aims to determine the energy shift and width of the kaonic deuterium $1s$ state induced by the strong interaction with precisions of 30 eV and 75 eV, respectively. However, this measurement is severely aggravated by the low kaonic deuterium X-ray yield. Due to this challenge, an improvement of the signal-to-background ratio by at least one order of magnitude compared to the previously performed kaonic hydrogen measurement (SIDDHARTA) is crucial.
This increase will be achieved in SIDDHARTA-2 through the implementation of three updates: a lightweight, cryogenic target, a newly developed large-area X-ray detection system consisting of Silicon Drift Detectors, and a dedicated veto system for background suppression. The veto system consists of an outer veto system (Veto-1) for active shielding and an inner veto system (Veto-2) for active shielding as well as the suppression of signal-correlated background in the form of charged particles. Excellent timing properties are required for both veto detectors.
The Veto-2 system was constructed, tested and optimised at the Stefan Meyer Institute. The time resolution, detection efficiency and its performance within a broad temperature range were studied and satisfying results were obtained. The first detector units of the Veto-2 system were installed in the SIDDHARTA-2 setup in Frascati.

Zusammenfassung

Im nicht-perturbativen, niederenergetischen Bereich der QCD wirft die Wechselwirkung zwischen Antikaonen und Nukleonen noch immer viele ungelöste Fragen auf und wird daher intensiv erforscht. Das Studium dieser $\overline{\mathrm{K}}$N-Interaktionen bietet Einsicht in die komplexen Prozesse der chiralen Symmetriebrechung und führt zu einem besseren Verständnis von fundamentalen Konzepten in der Hadronenphysik, wie etwa die Herkunft der Hadronenmassen.
Röntgenspektroskopie von kaonischen Atomen hat sich als vielseitges Werkzeug zur Untersuchung der starken Wechselwirkung bei niedrigen Energien erwiesen, da sie eine direkte Beobachtung des Einflusses derselben auf den Grundzustand kaonischer Atome ermöglicht. Das SIDDHARTA-2-Experiment, das derzeit am DAΦNE-Beschleunigerkomplex im italienischen Frascati gebaut wird, hat die Bestimmung der Energieverschiebung und der Breite des $1s$-Zustandes in kaonischem Deuterium mit einer Präzision von 30 eV beziehungsweise 75 eV zum Ziel. Diese Messung wird jedoch durch die für kaonisches Deuterium erwartete niedrige Röntgenausbeute bedeutend erschwert. Daher ist eine Verbesserung des Signal/Hintergrund-Verhältnisses um mindestens eine Größenordnung im Vergeich zu den vorhergehenden Messungen mit kaonischem Wasserstoff (SIDDHARTA) unbedingt erforderlich.
Diese Verbesserung in SIDDHARTA-2 basiert auf der Implementierung dreier Updates: eines leichten, kryogenischen Targets, eines neuentwickelten großflächigen Röntgendetektionssystems bestehend aus Siliziumdriftdetektoren und eines Vetosystems zur Hintergrundunterdrückung. Dieses setzt sich aus einem äußeren Vetosystem (Veto-1) zur aktiven Abschirmung und einem inneren Vetosystem (Veto-2) zusammen. Letzteres ist neben der aktiven Abschirmung auch für die Unterdrückung von signalkorreliertem Hintergrund, bestehend aus geladenen Teilchen, verantwortlich. Für beide Vetosysteme ist eine hervorragende Zeitauflösung essentiell.
Das Veto-2-System wurde am Stefan-Meyer-Institut gefertigt, getestet und optimiert. Seine Zeitauflösung, Nachweisempfindlichkeit sowie sein Verhalten in einem breiten Temperaturbereich wurden untersucht und zufriedenstellende Ergebnisse konnten erzielt werden. Ein erster Teil der Veto-2-Detektoreinheiten wurde im SIDDHARTA-2-Aufbau in Frascati installiert.

Acknowledgements

First and foremost, my deepest gratitude goes to Hannes. I want to thank you for all the incredible opportunities you provided, for your constant support, encouragement, and guidance not only in the lab, but also for the future. I greatly appreciate the time and effort you invested in me.

I also would like to express my appreciation to Eberhard for providing the opportunity to join SMI and his support and advice. At SMI, I was lucky enough to find a great team of colleagues and particularly want to thank Herbert, Michael and Julia as well as Leo, Doris and Mark, to whom I also want to offer my apologies. Moreover, I want to mention Carina, Constanze and Vici, without whom my time at SMI would have probably been only half as great. My special thanks also go to the entire team of SIDDHARTA-2, where I especially would like to express my gratitude to Catalina Curceanu for her support and counsel.

Furthermore, I owe deep gratitude to my support network at home. First, I want to thank Florian as well as the WINOs and Simon, who were always there and on whom I could always rely.
Finally, and most importantly, I need to thank my family. I would not be where I am without your constant support; without you, this would have never been possible.

Contents

1 Introduction

Although the strong interaction is one of the fundamental forces in nature, in the low-energy regime of quantum chromodynamics (QCD) many questions still remain unanswered. Particularly in bound state QCD dedicated studies are needed to shed light on these issues, one being the generation of the hadron masses which cannot be explained by the quark masses alone. The challenging difficulty of these experiments emphasises the opportunities presented by exotic atoms, providing a perfect environment for studying the strong interaction. Kaonic atoms in particular are ideal candidates as they are the lightest mesons containing a strange quark, allowing for a direct observation of the antikaon-nucleon interactions.

These interactions have been the subject of interest of several experiments performed at the Double Annular Φ-Factory for Nice Experiments (DAΦNE) collider in Italy as well as the Japan Proton Accelerator Research Complex (J-PARC) and the High Energy Accelerator Research Organisation (KEK) in Japan for years.
This thesis focuses on the Silicon Drift Detectors for Hadronic Atom Research by Timing Application (SIDDHARTA-2) experiment which will be performed at the DAΦNE collider complex at the Laboratori Nazionali di Frascati (LNF). In this experiment, kaonic deuterium atoms will be formed in a highly excited state; as the kaon releases its additional energy in a complex cascade process, it will approach the atomic nucleus close enough to be influenced by the nucleons' strong interaction. This interaction results in an energy shift and broadened width of the $1s$ ground state of the kaonic atom with respect to the solely electromagnetic value. SIDDHARTA-2 aims to directly observe this shift and width by measuring the X-rays emitted during the cascade process - particularly of the $2p$ to $1s$ transition - with precisions of 30 eV and 75 eV, respectively.

A combination of the results of the SIDDHARTA-2 experiment and its predecessors, the SIDDHARTA and DAΦNE Exotic Atom Research (DEAR) experiments, will enable for the first time the extraction of the isospin-dependent antikaon-nucleon scattering lengths a_0 and a_1, which are crucial inputs to further constrain the underlying theoretical models. In contrast to SIDDHARTA-2, DEAR and SIDDHARTA studied the $2p \rightarrow 1s$ X-ray transitions in kaonic hydrogen atoms and provided precise results on the $1s$ shift and width in the K^-p system.

However, the kaonic deuterium measurement proposed for SIDDHARTA-2 will have to face severe experimental challenges in the form of the very low kaonic deuterium X-ray yield and the high-radiation background in an accelerator environment. Only an increase of the signal-to-background ratio of at least one order of magnitude compared to SIDDHARTA will allow for a successful K^-d

experiment. Therefore, several measures to maximise the signal-to-background ratio will be implemented at SIDDHARTA-2, one of them being the installation of a dedicated veto system for background suppression. This thesis focuses on the Veto-2 system, which will be responsible for the minimisation of signal-correlated background originating from minimum ionising particles (MIPs) by the determination of the spatial correlation of simultaneous events in the X-ray detectors and the Veto-2 counters. A discrimination of this form of background is expected to increase the signal-to-background ratio by a factor of two.
The Veto-2 system was constructed and its performance studied at the Stefan Meyer Institute for Subatomic Physics (SMI) in Vienna. The results of this characterisation are presented in this work.

2 Kaonic Atoms

Exotic atoms are a form of matter in which negatively charged particles other than electrons, such as pions or antiprotons, form Coulomb bound states with the atomic nuclei. They were proposed in the 1940s (e.g. [1]) and first observed in 1951 in photographic emulsions [2]. They provide an excellent ground for testing nuclear properties and have since been heavily exploited in nuclear and particle physics. In the case of kaonic atoms, a negatively charged kaon (K^-) substitutes one electron in the atomic orbits and binds electromagnetically to the nucleus. Since kaons are the lightest mesons carrying strangeness, they are perfectly suited to study the strong interaction at low energies. Introducing a third quark flavour (up, down and strange), they allow to shed light on some of the most urgent unsolved problems in hadron physics, like the origin of the nucleon mass.

2.1 Formation and Properties of Kaonic Atoms

A kaonic atom is formed by the Coulomb capture of a negatively charged kaon with low kinetic energy by the atomic nucleus and the subsequent replacement of an outer shell electron by the K^-. The much higher mass of the kaon of 493.7 MeV/c^2 [3] compared to the electron mass of 0.5 MeV/c^2 [3] leaves the exotic atom in a highly excited state, as the principal quantum number n_{K^-} of the bound kaon is determined by

$$n_{K^-} \approx n_e \sqrt{\frac{\mu_{K^-}}{m_e}}, \tag{2.1}$$

where n_e denotes the principal quantum number of the outermost electron shell, m_e the electron mass and μ_{K^-} the reduced mass of the kaon and nucleus. Due to this excitation, a quantum cascade begins where the kaon releases its energy by transitioning into lower energy states. Depending on the atomic number of the exotic atom, different processes are dominant in the quantum cascade. For hydrogen and deuterium, the leading de-excitation processes are Coulomb de-excitation, Auger emission and, particularly for low-lying states, radiative decays, i.e. X-ray emission. The binding energies B_n of the energy states in the exotic atom are given in good approximation by the Bohr formula

$$B_n = \frac{\mu c^2 \alpha^2 Z^2}{2n^2}, \tag{2.2}$$

with μ being the reduced mass of the system, $\alpha \approx \frac{1}{137}$ the fine structure constant, Z the atomic number, c the vacuum speed of light and n again being the principal quantum number [4].
The cascade process in kaonic deuterium is shown in figure 1. Since the kaon, as a hadron, is subject to not only the Coulomb force but to the strong force as well, it interacts with the nucleons as soon as its n-state is in close proximity

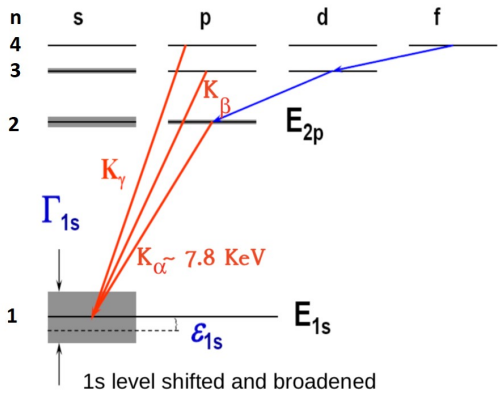

Figure 1: Schematic drawing of the cascade process in a kaonic deuterium atom. The shift ϵ_{1s} and width Γ_{1s} are determined by measuring the $2p \rightarrow 1s$ X-ray transition. *Picture courtesy of the SIDDHARTA-2 collaboration.*

to the nucleus. This hadronic potential influences the low-lying energy states of the exotic atom, with the ground state being influenced the most. The strong interaction induces an energy shift ϵ to the ground state, which can be determined by calculating the difference between the ground state energy resulting from the electromagnetic force, as given by equation 2.2, and the value observed by measuring K_α X-ray transitions from the $2p$ to $1s$ state in the kaonic atom:

$$\epsilon_{1s} = E_{2p\rightarrow 1s,measured} - E_{2p\rightarrow 1s,e.m.} \tag{2.3}$$

Furthermore, the strong interaction enables reaction channels for the kaon, which is finally absorbed by the nucleus from the ground state. This decrease of the state's lifetime τ leads to a broadening of the width Γ of this state ($\Gamma = \hbar/\tau$), observable as an increased Lorentzian line width of the X-ray transition.
One has to consider, following equation 2.4, that the kaon is located much closer to the nucleus than the electrons as a result of their higher mass. The exotic atom's orbital radii are approximated in leading order by the Bohr radii r_B

$$r_B = \frac{\hbar c}{\mu c^2 \alpha Z}, \tag{2.4}$$

where $\hbar$ corresponds to the reduced Planck constant [4]. Resulting from this relation, the dimensions of the exotic atom are much smaller compared to the electron-nucleus system. As the kaon reaches the low-n states, its orbital radius is much smaller than that of the electron in the corresponding state, leading to the kaonic atom system being very sensitive to nuclear interactions. On the one hand, this provides an ideal testing ground for studying these interactions; on the other hand, due to the kaon being influenced strongly by the nucleons,

absorption of the kaon from higher n-states with low angular momentum l is very likely, prematurely ending the cascade process and therefore reducing the $2p \rightarrow 1s$ X-ray yield. A more detailed description of the experimental challenges in these spectroscopic measurements is given in chapter 3.2.

2.2 $\overline{K}$N Scattering Lengths

A brief overview of the theory of the strong interaction, quantum chromodynamics and the process of chiral symmetry breaking, is given in the following section. This introduction draws upon the description provided by T. Hyodo and D. Jido in [5]. For simplicity, only the three flavour case, including the u, d, and s quark will be considered in the description.

QCD, the underlying theory of the strong interaction, "(...) is a color SU(3) gauge theory of quarks as fundamental fields and gluons as gauge fields" ([5], *page 7*). When removing the U(1) subgroups, the theory is left with $SU(3)_R \times SU(3)_L$ symmetry, which corresponds to chiral symmetry. This symmetry can be broken in mainly two ways, referred to as *explicit* and *spontaneous chiral symmetry breaking*. The latter is caused by the vacuum expectation value of the $q\overline{q}$ operator, which "(...) is not invariant under chiral symmetry, since it mixes the left- and right-handed quarks (...)" ([5], *page 7*). In the case of a spontaneous symmetry breaking, "(...) the spectrum of physical particles must contain one bosonic massless particle for each broken symmetry" ([5], *page 7*) as required by the Nambu-Goldstone theorem ([6], [7], [8]). The bosons created in this process are referred to as Nambu-Goldstone (NG) bosons and in the case of the three flavour model are the light pseudoscalar mesons π, K and η.
An explicit breaking of chiral symmetry is induced by the non-zero masses of the quarks, leading to the generation of small masses of the NG particles.
Non-perturbative effects of the strong interaction cannot be accurately described in chiral perturbation theory. Thus, for low energies, an effective Lagrangian considering the underlying symmetries can be constructed to reproduce the hadron scattering lengths. This can be achieved by the introduction of external fields to the QCD Lagrangian, using non-perturbative coupled-channel techniques, as described by Hyodo and Jido in [5], *pages 6-7*.

In general, this theoretical approach strongly depends on experimentally determined data to test predictions and constrain existing models. This input can be provided in terms of the isospin-dependent ($I = 0, 1$) complex scattering lengths a_0 and a_1 of the s-wave, characterising the $\overline{K}$N interaction at rest. Considering the kaonic deuterium system K^-d, the scattering lengths are connected to the $\overline{K}$N scattering lengths via

$$
\begin{aligned}
a_{K^-p} &= \frac{1}{2}[a_0 + a_1] \\
a_{K^-n} &= a_1 \\
a_{K^-d} &= \frac{4[m_N + m_K]}{[2m_N + m_K]}Q + C \\
Q &= \frac{1}{2}[a_{K^-p} + a_{K^-n}] = \frac{1}{4}[a_0 + 3a_1],
\end{aligned}
\tag{2.5}
$$

where a_{K^-p}, a_{K^-n} and a_{K^-d} stand for the scattering lengths of a K^- interacting with a proton, neutron and deuterium atom, respectively. m_N denotes the nucleon mass, m_K the kaon mass, and C corresponds to a correction term for higher-order contributions from three-body interactions.
As described earlier, the observables of interest in kaonic atom spectroscopy are the energy shift ϵ_{1s} and the broadened width Γ_{1s} of the ground state of the kaonic atom. A precise observation of these ground state modifications in kaonic deuterium allows for the determination of the $\overline{\text{K}}$N scattering lengths, as they are interrelated through

$$
\epsilon_{1s} - \frac{i}{2}\Gamma_{1s} = -2\alpha^3\mu_c^2 a_{K^-d}(1 - 2\alpha\mu_c(ln(\alpha) - 1)a_{K^-d}) \tag{2.6}
$$

with α being the fine structure constant and μ_c the reduced mass of the K^-d system [9]. Equation 2.6 is an improved version of the original work formulated for pionic atoms by Deser *et al.* in 1954 [10], which is necessary due to the large isospin breaking contributions in kaonic atoms. This equation correlates the observables ϵ_{1s} and Γ_{1s} with the K^-d scattering length; for the kaonic hydrogen case, an analogous relation holds. Resulting from equations 2.5 and 2.6, for the extraction of the isoscalar a_0 and the isovector a_1, a combination of the results from kaonic hydrogen and kaonic deuterium measurements is needed. Several kaonic hydrogen measurements have been performed to determine precisely the a_{K^-p} scattering length, located at the LNF in Italy and J-PARC and the proton synchrotron at KEK (KEK-PS) in Japan. Figure 2 compares the results obtained in the DEAR, SIDDHARTA and KEK-PS E228 experiments for the shift and width of the kaonic hydrogen ground state.
From SIDDHARTA's well-understood kaonic hydrogen results, constraints on the complex forward scattering amplitude could be derived, which are shown in figure 3.
The theoretical predictions for the kaonic deuterium energy shift ϵ_{1s}, the width Γ_{1s} and the a_{K^-d} scattering length are listed in table 1. Further experimental input clearly is needed, as the calculated values vary significantly. For this reason, a precise determination of the ground state modifications in kaonic deuterium is crucial, necessitating the performance of the SIDDHARTA-2 experiment.

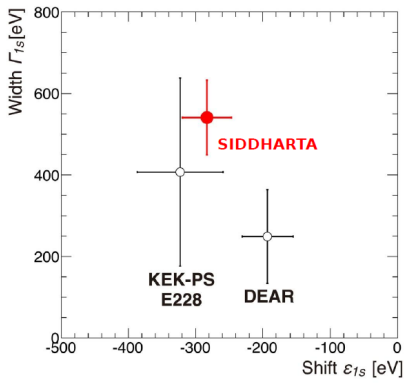

Figure 2: Comparison of the results for the induced shift and width of the kaonic hydrogen ground state obtained by the DEAR [11], SIDDHARTA [12] and KEK-PS E228 [13] experiments. *Picture taken from* [14].

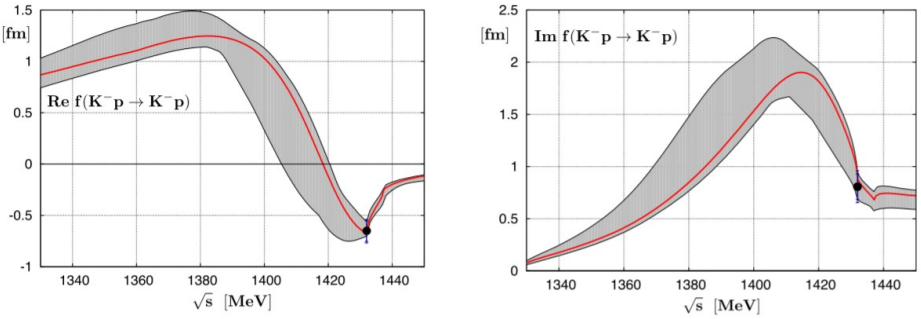

Figure 3: Anaylsis on the real and imaginary part of the $K^-p \to K^-p$ forward scattering amplitude, together with the experimental data obtained in the SIDDHARTA experiment shown by the dots. $\sqrt{s}$ stands for the meson-baryon centre-of-mass energy. *Picture taken from* [9].

ϵ_{1s} (eV)	Γ_{1s} (eV)	a_{K^-d} (fm)	Reference
-670	1016	$-1.42 + i1.60$	Weise *et al.* (2017) [9]
-887	757	$-1.58 + i1.37$	Mizutani *et al.* (2013) [15]
-787	1011	$-1.48 + i1.22$	Shevchenko (2012) [16]
-779	650	$-1.46 + i1.08$	Meißner *et al.* (2011) [17]
-769	674	$-1.42 + i1.09$	Gal (2007) [18]

Table 1: Theoretical calculations of the expected values for the energy shift ϵ_{1s} and width Γ_{1s} of the ground state in kaonic deuterium as well as the prediction for the kaonic deuterium scattering length a_{K^-d}.

3 The SIDDHARTA-2 Experiment

3.1 The History of Kaonic Atom Measurements: DEAR and SIDDHARTA

Located at the DAΦNE collider at the LNF, the DEAR experiment performed there a first precision measurement of the shift and width of the ground state of kaonic hydrogen [19] by observing $2p$ to $1s$ X-ray transitions. DAΦNE is a positron-electron collider operated at the centre of mass energy of the Φ meson of 1.02 GeV [20]. Therefore, the mesons are produced with negligible kinetic energy and decay into kaon-antikaon pairs emitted back-to-back with a branching ratio of around 49% for charged kaon pairs [21], providing a unique low-momentum, monochromatic beam of antikaons.

As the successor to DEAR, the SIDDHARTA experiment aimed to measure again the $1s$ shift and width in kaonic hydrogen with even higher precision. In contrast to the charge-coupled devices (CCDs) used in DEAR, SIDDHARTA implemented Silicon Drift Detectors (SDDs) for the detection of the K_α transition X-rays of kaonic atoms. The large background prominent during DEAR resulted in a poor signal-to-background ratio and limited the precision of the measurements. Therefore, the switch to fast, triggerable SDDs in SIDDHARTA was motivated by the possibility of using timing information to distinguish between background events and "real" X-ray events and hence to drastically suppress background [22].

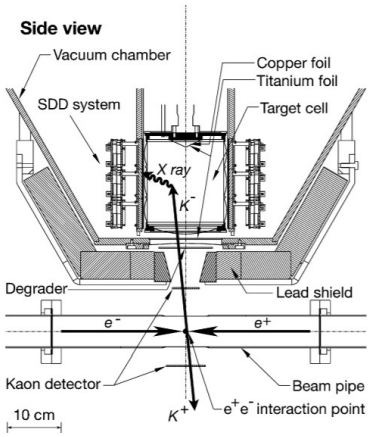

Figure 4: Schematic view of the SIDDHARTA setup. *Picture taken from* [23].

SIDDHARTA implemented a kaon trigger system correlated to the entrance of the antikaons into the target. To optimise the stopping of the negative kaons, the target had to be lightweight and operated at cryogenic temperatures and was filled with gaseous hydrogen or deuterium, respectively. The SIDDHARTA setup is shown in figure 4, taken from [23]. In this way, the experiment was

taking data for six months in 2009 and the kaonic hydrogen K_α transition shift and width were obtained with unprecedented precision, where the given uncertainties are the sum of statistical and systematic errors [12]:

$$\epsilon_{1s} = -283 \pm 42 \text{ eV}$$
$$\Gamma_{1s} = 541 \pm 111 \text{ eV}$$

In addition to the K^-p measurements, SIDDHARTA also studied the shift and width of the $2p$ states in ^{3}He and ^{4}He ([24], [25]). Furthermore, first studies of the kaonic deuterium yield have been performed [26]. Following the SIDDHARTA experiment, SIDDHARTA-2 will allow for the first time the extraction of the isospin-dependent ($I = 0, 1$) antikaon-nucleon scattering lengths a_0 and a_1. In order to obtain also the antikaon-neutron scattering length K^-n (a_1) the kaonic deuterium measurement is needed in combination with the kaonic hydrogen results, as described in chapter 2.2. SIDDHARTA-2 aims to determine the kaonic deuterium ground state shift and width with precisions of 30 eV and 75 eV, respectively.

3.2 Experimental Challenges

The experimental challenge for the SIDDHARTA-2 experiment is the low kaonic deuterium X-ray yield Y_{K^-d} combined with the high background expected in an accelerator environment. Preliminary studies for the K^-d X-ray yield have shown the upper limit for the total yield to be $Y_{K^-d} = 0.4\%$ [26]; Monte Carlo (MC) calculations expect the K_α yield for SIDDHARTA-2 to be 0.1%, meaning that only 0.1% of the kaons stopped in the target gas actually reach the ground state of the kaonic atom. Compared to kaonic hydrogen, this corresponds to a difference in X-ray yields of one order of magnitude.
One of the aspects leading to this low yield, well known from kaonic hydrogen, is the Stark effect. This effect describes the mixing of states with the same principal quantum number n but different angular momenta l of atoms in an external electric field. The electric field seen by the kaonic atom is originating from the other target atoms, resulting in a strong dependence of the effect of Stark mixing on the target gas density. Due to the mixing of l-states to lower l-states, absorption of the kaon from even higher n-levels becomes more likely.

Another effect specific to K^-d is induced by the presence of the neutron. The addition of another nucleon also increases the probability of kaon absorption from higher n- and low-l-states due to a larger overlap of wavefunctions. This prevents the kaon from reaching the ground state and significantly reduces the kaonic deuterium X-ray yield in comparison to kaonic hydrogen.

In order to increase the signal-to-background ratio and therefore enable a successful kaonic deuterium measurement, precise knowledge of the background is

crucial. Detailed background studies have been performed with the information gained during the kaonic hydrogen measurements in previous experiments [14]. One can distinguish between "synchronous" and "asynchronous" background with respect to their correlation to the kaon trigger. The "synchronous" background consists mostly of hadrons and originates from nuclear absorption during the cascade process or the decay of the antikaon. The "asynchronous" background component however results from particle showers induced in the setup by the colliding e^-/e^+ beams of DAΦNE [14]. With this knowledge, the final SIDDHARTA-2 setup could be optimised.

In summary, an upgrade of the SIDDHARTA apparatus is essential for the successful performance of the SIDDHARTA-2 experiment, based on three main pillars [27]:

- A lightweight cryogenic target cell with Kapton sidewalls with a thickness of about 150 μm and a working temperature of 30 K, allowing for a transmission of 90% of 8 keV X-rays.
- A compact, large area X-ray detector system with high efficiency and high resolution as well as stable operating conditions. This detection system consists of SDDs, resulting in an active area of 246 cm^2.
- A dedicated veto system for the improvement of the signal-to-background ratio of at least a factor of ten. The veto system is comprised of two components, the Veto-1 and the Veto-2 system. The Veto-1 works as active shielding, using timing information to distinguish kaon stops in the target gas from kaons stopped in the entrance window or sidewall of the target. In comparison to the time a kaon needs to be stopped in the surrounding setup, the stopping time in gas is much longer. This information can thus be used to suppress one component of the background originating from "false" kaon stops. MC calculations have shown that a time resolution of < 500 ps is needed for the veto system. In addition, the Veto-2 system can also be used as active shielding and act as support of the Veto-1, increasing the active area. Furthermore, the Veto-2 is dedicated to suppress beam-correlated background coming from MIPs originating from the nuclear kaon absorption by determining the spatial correlation between particle hits in the SDDs and in the Veto-2 [27].

3.3 Experimental Setup of SIDDHARTA-2

SIDDHARTA-2 will be located at the interaction point of the DAΦNE collider at the LNF, the same site as used for SIDDHARTA. A schematic view of the setup can be seen in figure 5(a). The entire setup will be mounted on a specifically designed frame and table. A luminosity monitor, the luminometer, is placed horizontally on both sides of the beam pipe. SIDDHARTA-2 is expected to accumulate data with an integrated luminosity of 800 pb^{-1}. The

kaon trigger system consists of two plastic scintillators with photomultiplier tube (PMT) read-out, with one scintillator mounted underneath the interaction point and the second one directly in front of the entrance window to the vacuum chamber above the beam pipe. Since the K^- at DAΦNE have very low momenta, a few millimetres of plastic degrader are sufficient to stop the maximum amount of kaons in the target gas.

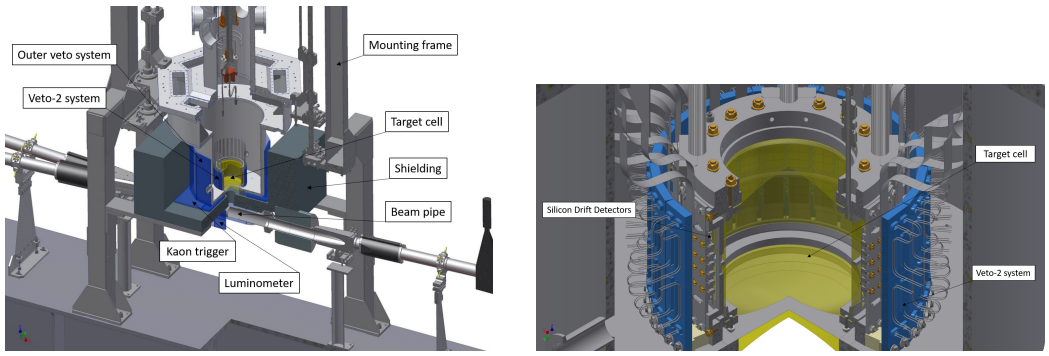

(a) Schematic view of the experimental setup of SIDDHARTA-2.

(b) Detailed view of the target cell with SDDs and Veto-2 counter.

Figure 5: Experimental setup of SIDDHARTA-2: vacuum chamber, detectors and target cell. *Picture courtesy of SMI Vienna.*

After the antikaons are slowed down, they can be stopped in the cryogenic target cell mounted inside the vacuum chamber (figure 5(b)), which is filled with gaseous deuterium, and kaonic deuterium atoms will be formed. The sidewalls of the target cell consist of two layers of 50 μm Kapton foil glued together, resulting in a sidewall thickness of $\sim$ 150 μm. A 2-stage closed-cycle He cooler is responsible for the cooling of the target cell, two CryoTigers are dedicated to cool down the SDDs. For a detailed description of these components, see chapter 6.

As described in the previous section, the density of the deuterium gas inside the target cell has to be optimised for the maximisation of the kaonic deuterium X-ray yield, balancing between losses due to the Stark effect and the highest kaon stopping power. The chosen gas density is 5% of the liquid deuterium density (LDD), with a working pressure of 0.3 MPa at 30 K [14].

Surrounding the target cell, 48 arrays of SDDs are mounted for the detection of the kaonic X-rays, resulting in a total of 384 read-out channels. The SDDs are operated at a temperature of approximately 120 K. The Veto-2 system is placed directly behind the X-ray detectors, as shown in blue in figure 5(b). The Veto-1 counter, consisting of an outer ring of scintillators with PMT read-out, is mounted outside the vacuum chamber. Figure 6 shows the setup of the components inside the vacuum chamber as well as the electronics for the power supply and read-out of the detectors outside.

Due to the high radiation background in DAΦNE, passive shielding in the form of lead bricks is placed on the mounting table behind the Veto-1 system as well as underneath the vacuum chamber, in addition to the active shielding

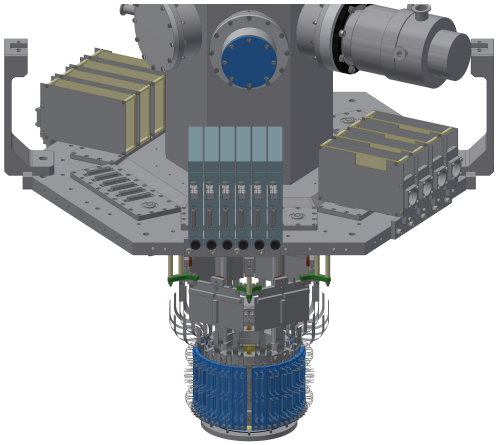

Figure 6: Schematic drawing of the detectors inside the SIDDHARTA-2 vacuum chamber together with the electronics outside. *Picture courtesy of SMI Vienna.*

provided by the veto systems.

3.4 The Veto-2 System

As described before, the Veto-2 system is mainly responsible for the suppression of signals originating from MIPs. These charged particles can produce signals in the SDDs mimicking a real X-ray event in multiple scenarios, displayed in figure 7.

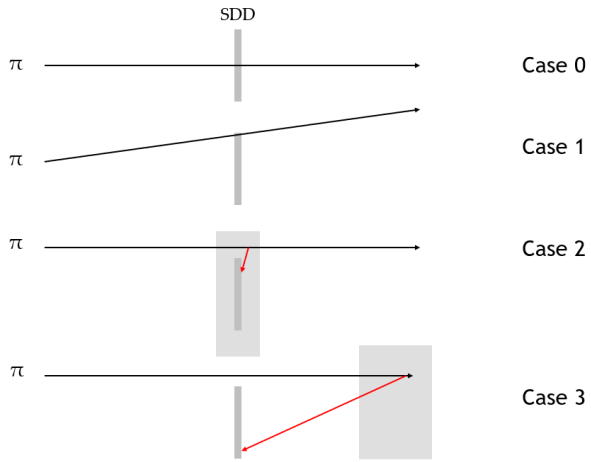

Figure 7: Different scenarios contributing to the signal-correlated background in SIDDHARTA-2.

If the MIPs directly hit the SDDs (case 0), the charge deposition in the detectors depends on the position of the particle traversing. Should the MIP pass the SDD within its active area, the signals produced can be rejected immediately as their energy is much higher than the X-ray region of interest. However, if the SDDs are traversed outside near the edge of their active area (case 1), far less charge is deposited and the resulting signal could be interpreted as a real

X-ray event.
This is also the case if the mounting structure of the SDDs is hit by charged particles and delta-rays are produced close to the detectors, reaching the SDDs' active area (case 2). Also, secondary X-rays or backscattered electrons originating from the setup surrounding the SDDs could be detected as well, with their signals being misinterpreted as X-ray signals (case 3).
All of these processes contribute to a signal-related background which cannot be rejected by using timing information, but rather by determining the spatial correlation of particle events in the SDDs and the Veto-2 counters mounted directly behind them. Since interesting X-ray signals detected by the SDDs will not reach the veto system, every event registered in the Veto-2 as well as the corresponding SDD within a certain time window can be dismissed as MIP-related background. The time window for the coincidence in the Veto-2 and the SDDs is determined by the drift time of the electrons in the SDDs, with the kaon trigger operating as start signal.
MC calculations have shown that the discrimination of the signal-correlated background via the Veto-2 system will increase the signal-to-background ratio by a factor of two [14].

4 Components and Construction of the Veto-2 System

4.1 Silicon Photomultipliers

In the beginning of the twenty-first century, Geiger-mode avalanche photodiodes (G-APDs) were developed. Since these devices are able to detect single photons similar to a PMT, they are often referred to as silicon photomultipliers (SiPMs). In addition to their high photodetection efficiency, they also feature an internal gain comparable to a PMT and very good timing properties. Moreover, they operate stably in magnetic fields.
Their working principle is derived from solid-state pin-diodes, where "pin" describes their structure consisting of a p-doped, an intrinsic-p (p_i, p^-), and an n-doped region. Avalanche photodiodes have a similar structure, but with an additional highly doped n- or p-layer acting as multiplication zone, responsible for the avalanche effect in the diode. A typical configuration of a G-APD is n^+-p^+-p_i-p^+ (figure 8). They are operated with reverse bias voltage above the breakdown voltage (Geiger-mode), leading to the high internal gain (10^5 - 10^7) and high signal-to-noise ratio, therefore enabling the single photon detection [28].

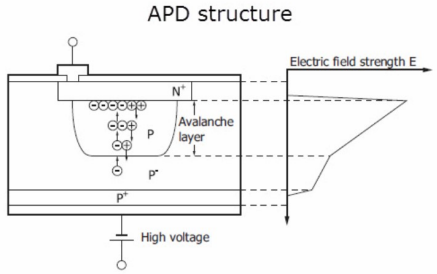

Figure 8: Structure of an avalanche photodiode with electric field configuration. The multiplication zone is formed by the p-n^+ junction. *Picture taken from* [29].

A SiPM consists of an array of parallelly connected square-shaped microcells, where each microcell is comprised of a G-APD and a resistor R_{quench} for active quenching (figure 9). All microcells are connected to a common cathode and a common anode output.

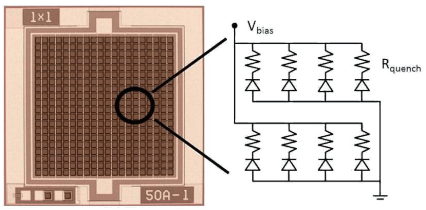

Figure 9: Internal structure of a SiPM. *Picture taken from* [30].

The amplitude A_i of the signal produced by a microcell is proportional to the capacitance C of the cell as well as the applied overvoltage:

$$A_i = C(V - V_B), \tag{4.1}$$

where V denotes the bias voltage applied to the cell and V_B the breakdown voltage.
The output signal A of the SiPM is the sum of the signals from all firing cells:

$$A = \sum_i A_i. \tag{4.2}$$

The SiPMs used for the veto system are manufactured by AdvanSiD in Trento, Italy, and operate in the near-UV range with a peak photon detection efficiency at 420 nm. They feature an active area of 4×4 mm^2 with 9340 microcells of size 40×40 μm^2 [31]. A bias voltage of approximately 30 V is sufficient for the operation of the SiPMs.

4.2 Scintillators

A scintillator is a luminescent material producing light when struck by ionising radiation. The principle of scintillation is based on the absorption of the energy of the incident radiation, therefore exciting the atoms or molecules of the material, and the subsequent re-emission of this energy in the form of scintillation light.

Depending on the desired application, different types of materials are favourable. In general, one can distinguish between organic and inorganic scintillators. Inorganic scintillators are typically crystals or glasses, whereas organic scintillators are liquids or plastic scintillators. The latter usually consist of more than one component, a fluor and a base. The fluor refers to the primary emitter of scintillating light (fluorescence), which is immersed in a solid polymer base consisting of aromatic hydrocarbon compounds, serving as supporting structure. Plastic scintillators are widely used in nuclear and particle physics due to their fast fluorescence process, high light output, low cost, and mostly their easily adaptable geometry.

The scintillators used for the Veto-2 system are plastic scintillators of the type EJ-200 with a polyvinyltoluene base, manufactured by Scionix Holland and of size $50 \times 12 \times 4$ mm^3. Their maximum emission wavelength is 425 nm, chosen to match the SiPMs [32].

4.3 Veto-2 System Detector Units

The Veto-2 system consists of 96 units of scintillators and SiPMs. One SiPM is attached to the short side of each scintillator with a clear epoxy adhesive.

To transport the output of the SiPM to the electronics, twisted pair cables of 125 cm length are used (figure 10(a)). The detector tiles are placed in 24 black, 3D-printed boxes, which are mounted directly behind the SDDs on the target cell (figure 10(b)).

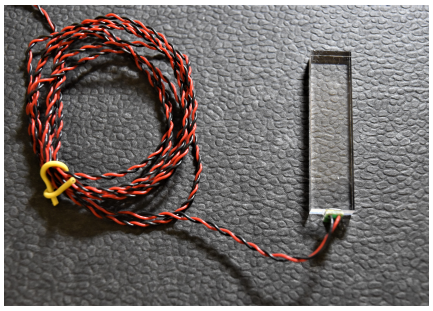

(a) Detector unit consisting of the scintillator with attached SiPM.

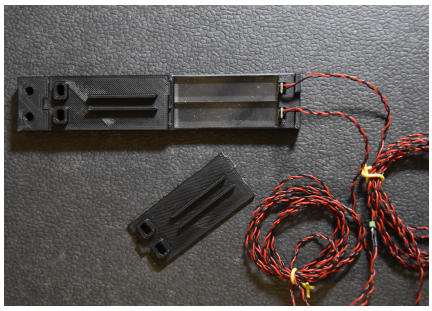

(b) Two detector units placed in a 3D-printed box.

Figure 10: Detector units of the Veto-2 system.

As a first step during the construction process, twisted pair cables with a length of 125 cm were soldered to the SiPM boards. Different cable lengths were tested and it was concluded that cables with a length of up to 125 cm would not negatively influence the performance of the SiPMs and the signal-to-noise ratio. After a first installment of veto counters in the SIDDHARTA-2 setup (see chapter 6), the cables were shortened to a length of 70 cm.
For the process of gluing the SiPMs to the scintillators, fixtures for both of them were 3D-printed (figure 11(a)) to facilitate the gluing and to ensure stable quality for each of the 96 modules. After cleaning the scintillators and SiPMs with isopropanol, the SiPMs were placed in the fixtures. The adhesive was applied to the diodes and the scintillators were held in place using small clamps.

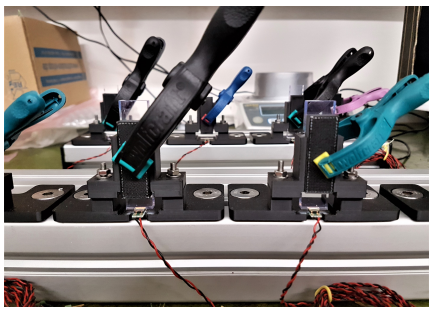

(a) SiPM and scintillator in fixture during gluing process.

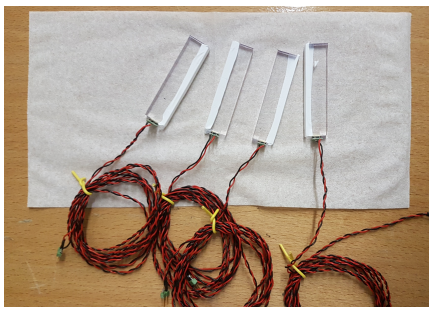

(b) Scintillator tiles with teflon layer.

Figure 11: Construction of the Veto-2 detector units.

The adhesive used is a clear, two component epoxy with good optical properties (EPO-TEK ® 301). The mixing ratio of the components is 20:5. Following the mixing of the two constituents, the mixture needs approximately twenty

minutes to become viscous and therefore ready to apply to the SiPMs. After a period of 24 hours, the adhesive is cured and the SiPMs are firmly attached to the scintillator tiles. During this gluing process, it has to be ensured that no air is trapped in the adhesive in the form of bubbles as this will negatively influence the connection between the SiPM and the scintillator and decrease the light transmission.

In order to diminish any crosstalk between the scintillator-SiPM tiles, two layers of teflon tape were placed on the touching sides of each pair of scintillators before placing them into their black housings (figure 11(b)). Each housing contains four scintillator tiles. For a more detailed description of the crosstalk elimination, see chapter 5.1.
The black housing boxes were printed using acrylonitrile butadiene styrene (ABS). They were permanently closed using a black epoxy adhesive (Aremco-Bond-2310), which was also used to fix part of the cables to the box as a strain relief.

4.4 Electronics

4.4.1 Amplification Boards

For the control and read-out of the SiPMs, dedicated amplification boards were manufactured at SMI. The boards provide twelve input channels as well as twelve analogue and digital output channels each. In total, eight boards are used for the amplification of all SiPMs for the SIDDHARTA-2 experiment.

Each board features twelve high voltage (HV) modules for the bias voltage supply of the silicon diodes. The gain, i.e. the bias voltage, can be adjusted separately for each channel by regulating the dark current, which can be measured on the current port (figure 12). For the SIDDHARTA-2 boards, the bias voltage can be chosen within a range of < 10 and > 35 V. The analogue output delivers the differential signal of the amplified negative SiPM pulse. The digital output provides a time-over-threshold (ToT) signal, with its width determined by the threshold set with a discriminator for each channel. Consistent with the analogue signal, the ToT output is in the form of a Low Voltage Differential Signal (LVDS). Due to the differential and LVDS output, respectively, the pick-up of noise from the detectors to the amplification boards can be drastically reduced by using twisted pair cables.

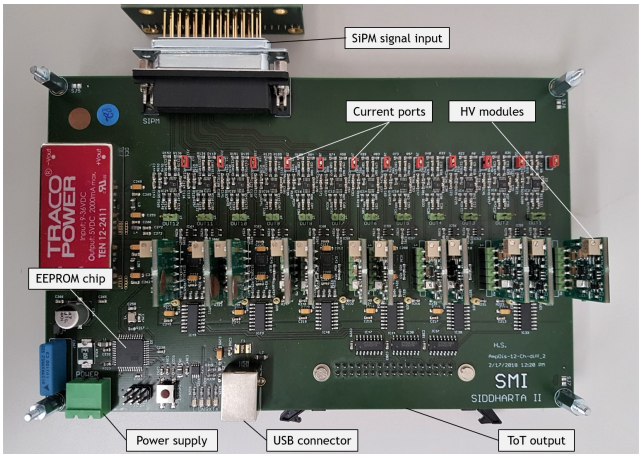

Figure 12: Twelve-channel IFES amplification board for SIDDHARTA-2.

The electronics used for these boards is the Intelligent Front end Electronics for Silicon photo detectors (IFES), which was developed at SMI for the purpose of remote-controlling and operating SiPMs. Its block diagram (figure 13) shows the three different parts of the system. Part A is responsible for the bias supply of the detector featuring a constant current source with Boost-Converter, the differential amplification of the analogue SiPM signal, and the comparator for the digital signal. Part B consists of the power supply and part C accommodates the control bus and Digital-to-Analogue Converter (DAC) connections [33].

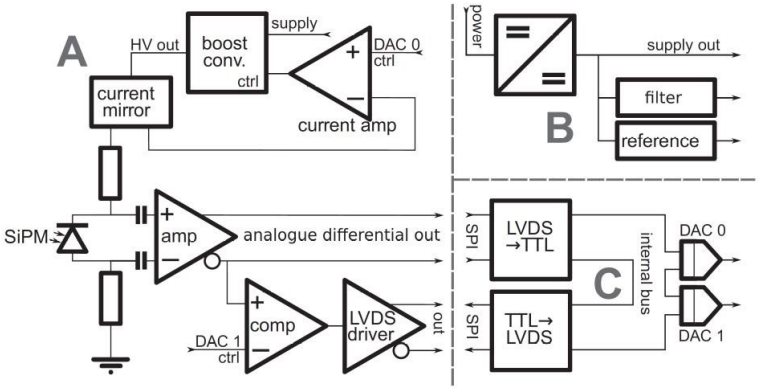

Figure 13: Block diagram for the IFES electronics. *Picture taken from* [33].

Both the current source (i.e. the gain) as well as the comparator threshold can be adjusted remotely via an Electrically Erasable Programmable Read-Only Memory (EEPROM) chip implemented on each board. Using a Python-based Graphical User Interface (GUI), which is shown in figure 14, the channel settings are easily accessible via a simple Universal Serial Bus (USB) connection and can be set to values between 0 and 4095.

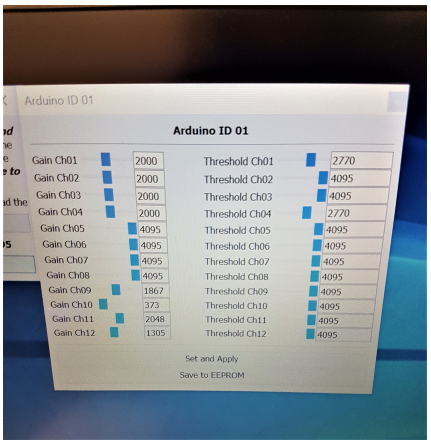

Figure 14: GUI for setting the gain and threshold for each channel.

4.4.2 Data Acquisition System

To transport the digital signal from the amplification boards to the data acquisition (DAQ) system, twisted pair flat cables are used. Since only the digital ToT signals are needed, a Time-to-Digital Converter (TDC) (CAEN 128 Channel Multihit TDC V1190A) is used for the DAQ.
The kaon trigger system provides a start signal.

5 Characterisation

5.1 Crosstalk Minimisation

In order to avoid the false rejection of X-ray signals in the region of interest, the crosstalk between neighbouring detectors inside their black encasements had to be minimised. Therefore, a crosstalk evaluation was performed using a Cs-137 source to irradiate the scintillators on up to three different positions (figure 15). The pulse height spectra were measured with the oscilloscope LeCroy WaveRunner 625Zi for the probed detector unit as well as its direct neighbour, with the trigger set on the directly irradiated detector. From the obtained spectra the crosstalk probability was calculated as the fraction of the total sum of events in the detector without source and the sum of events in the irradiated detector. Multiple shielding techniques and materials were tested to find the optimal configuration.

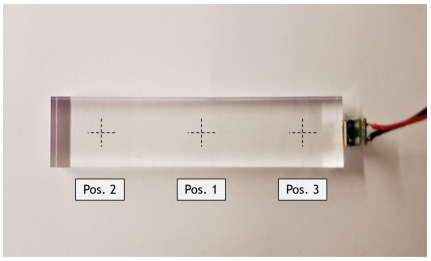

Figure 15: Positions on the scintillator irradiated with the Cs-137 source to determine the crosstalk probability of the detector units.

For calibration, the detector units were positioned apart from one another and the source, collimated to 2 mm, was placed on one scintillator. Since the SiPMs should not be reached by broad light, the entire setup was installed in a blackbox made of carton, lined with black velvet-faced paper and black tape to ensure it was light-tight (see figure 16). The pulse height spectra for both SiPMs were measured. As expected, no coincidences of signals in both detectors, i.e. no crosstalk, was observed in this way.
After this, the detectors were placed side by side in their black housing without any shielding layer between them, and position 1 of one scintillator was irradiated by the collimated Cs-137 source. Now, a crosstalk probability of $(0.63 \pm 0.02)\%$ was observed.
Next, a sheet of aluminium foil was wrapped completely around one detector unit. At first, the source was placed on the wrapped scintillator and the pulse height spectra were measured for the three positions described. As a cross-check, however, the source was then placed onto the "naked", unwrapped neighbouring scintillator on the same three positions and the results of both configurations were compared. Table 2 lists the evaluation results for all dif-

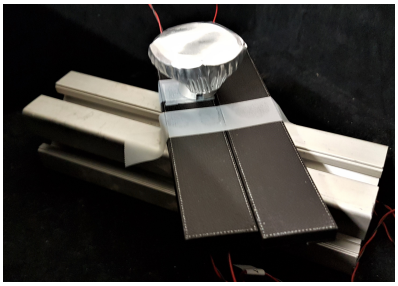

Figure 16: Collimated source placed on the detector unit inside the light-tight blackbox.

ferent tested configurations. For this setup, the results differ significantly for the two scintillators. When the source was placed on the scintillator wrapped in aluminium foil, in some cases an event was detected in the neighbouring scintillator as well. This was not the case, however, if the source was placed on the unwrapped scintillator, since no crosstalk events were obtained in this way. This behaviour could be explained by small holes or slits in the aluminium, allowing for light to escape from inside the wrapping more easily than for it to enter from the outside of the wrapping. The aluminium foil possibly reflected the light multiple times, increasing the probability for it to reach the other scintillator through the slit.

To sum up, as table 2 shows, shielding the detectors with aluminium foil did not lead to satisfying results, and other materials were tested.
At first, the touching sides of the scintillators were covered with white correction tape consisting of polyester. One position on each scintillator was irradiated to determine the crosstalk probability. With this method, no crosstalk events were observed anymore. However, the application of the tape to the scintillators proved to be difficult, since the tape is not durable and rips easily, impeding the complete coverage of the scintillator.

Method	Position	CP Scint. 1 (%)	CP Scint. 2 (%)
Al foil on scint. 1	1	0.54 ± 0.01	0.00 ± 0.07
	2	0.60 ± 0.02	0.00 ± 0.10
	3	0.54 ± 0.02	0.00 ± 0.04
Correction tape	1	0.00 ± 0.07	0.00 ± 0.08
Teflon tape	1	0.00 ± 0.07	0.00 ± 0.10

Table 2: Different configurations tested to minimise the crosstalk between the neighbouring detectors scintillator 1 and scintillator 2. Columns 3 and 4 correspond to the crosstalk probability (CP) obtained for the listed scintillator irradiated with the Cs-137 source.

Hence, the method of choice was to cover the touching sides of the neighbouring scintillators with a thin teflon tape, as this resulted in a vanishing crosstalk probability as well (table 2), but was much easier to handle and to apply to the

detectors. The final configuration chosen for the Veto-2 system was therefore to cover the touching narrow sides of each scintillator with this teflon tape to fully eliminate the crosstalk between neighbouring detector units.

5.2 Time Resolution

MC calculations require the time resolution of the veto system to be better than 500 ps for the distinction between kaon gas stops or stops in the setup. Thus, the time resolution of the Veto-2 system was determined. For this, a diode laser (OSRAM) with a wavelength of 450 nm was used to irradiate the surface of a scintillator tile with SiPM attached [27]. The detector units were placed in an open, 3D-printed housing box, which was mounted on a movable aluminium structure to vary the irradiation positions; whereas the diode, once clamped into the fixture and adjusted, was to be held at a constant position. This configuration is shown in figure 17.

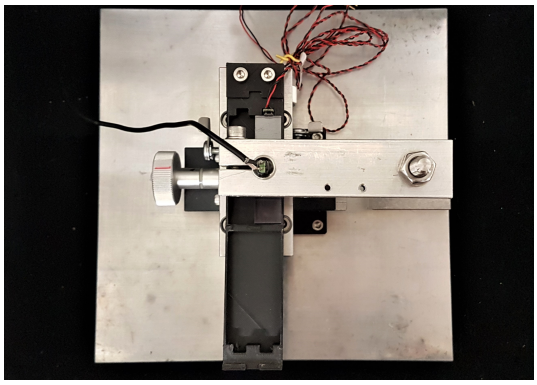

Figure 17: Experimental setup used for the determination of the detectors' time resolution. The fixture to hold the detectors and the diode laser was placed inside a blackbox.

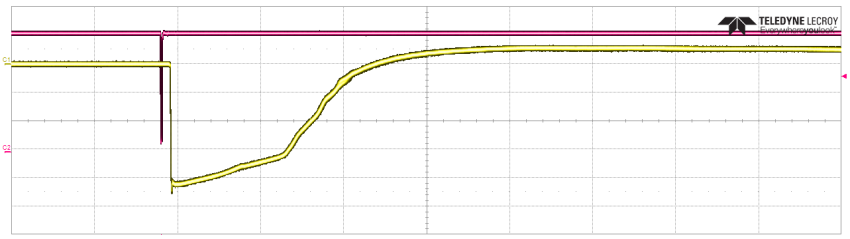

Figure 18: Oscilloscope recording of the time delay between diode laser pulse (pink) and SiPM signal (yellow). The time scale is 200 ns/div, the voltage scale for the SiPM signal is 200 mV/div.

The laser was operated in a pulsed mode with square pulses and a frequency of 230 Hz using a Keysight 81160A Pulse Function Arbitrary Generator to measure the time delay between the laser pulse and the SiPM signal. To operate the SiPM and amplifier in saturation and, more importantly, minimise

the jitter of the laser pulse rise time, a configuration of the laser power with an amplitude of 4.2 V and a width of 2.8 ns was chosen. In this way, the time delay could be determined using only a simple threshold trigger [27]. An example of an oscilloscope recording of the saturated signal of the SiPM as well as the diode pulse is shown in yellow and pink, respectively, in figure 18. The oscilloscope used for this and the measurement of the time delay was a LeCroy WaveRunner 625Zi.

On each scintillator, three or five different positions were probed with the laser, which are shown in figure 19(a). The three positions centred longitudinally along the scintillator tile were irradiated each time, whereas the two additional positions were shifted with respect to the centre to determine the homogeneity of the material.

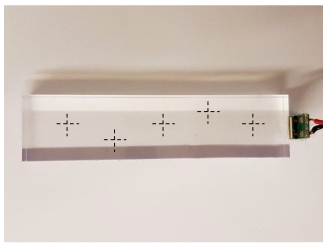

(a) Laser probing positions on the scintillator tile. *Picture taken from* [27].

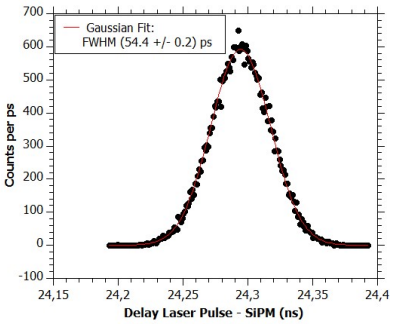

(b) Data set with applied Gaussian fit (red) and obtained FWHM of (54.4 ± 0.2) ps. *Picture taken from* [27].

Figure 19: Laser positions and observed data set for one scintillator with Gaussian fit.

A Gaussian fit was applied to the obtained time delay distributions and the Full Width Half Maximum (FWHM) was calculated for each position to determine the corresponding time resolution. An example of one data set can be seen in figure 19(b).
The mean value was calculated including all measurements for all positions on each scintillator, which are shown in figure 20. In this way, a result of $(54.0 \pm 0.1_{stat} \pm 2.0_{syst})$ ps was obtained [27]. In comparison to the minor statistical uncertainty arising from the Gaussian fit, the systematic uncertainty, correlating to the scattering of the data points around the mean value in figure 20, clearly dominates. Imperfections of the scintillators, including surface irregularities leading to the scattering of the laser light as well as inhomogeneously distributed colour collection centres inside the material, could have resulted in a loss of light collection and therefore contributed to the systematic uncertainty of the time resolution. Another possible source of error would be

the positioning of the diode laser with respect to the scintillator, influencing the incident angle of the probing radiation.

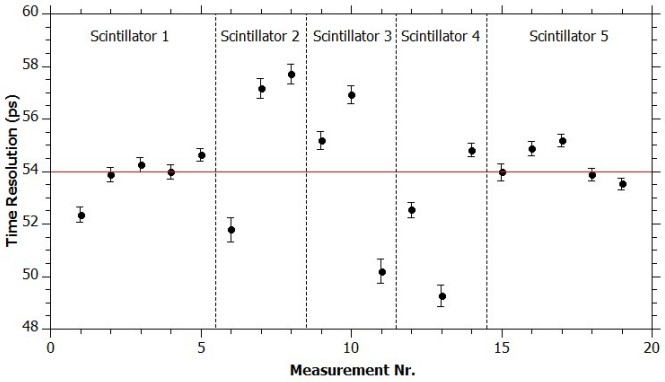

Figure 20: Time resolution for each measured position on different scintillators. The calculated mean is shown in red. *Picture taken from* [27].

Due to the considerable scattering of the data points around the mean value, a dependence of the time resolution on the irradiation position of the laser was indicated. Therefore, the data was analysed in order to look for a correlation between the time resolution and path length travelled by the light through the scintillator for each position. However, no systematic trend was found as shown in figure 21 for different scintillators [27].

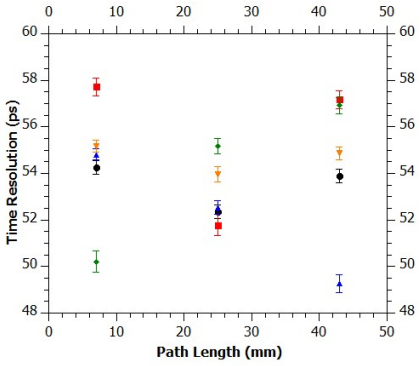

Figure 21: Time resolutions obtained for different positions in dependence of the covered laser path length. Different colours correspond to different scintillator tiles. *Picture taken from* [27].

When the drift times of the laser light through the scintillator material are taken into consideration for the different positions, an average resolution of 293 ps with a standard deviation of 45 ps was obtained. Since this result was better than the required 500 ps by a factor of 1.7, no attempt for the improve-

ment of the setup and hence the decrease of the systematic uncertainty was made. It can be concluded that the Veto-2 system can be used for the suppression of background relating to kaon stops in the target window or sidewall in addition to the suppression of MIP-related background. Furthermore, the outcome of this measurement indicates a high-quality and stable production process of the scintillator-SiPM tiles.

5.3 Detection Efficiency

To increase the signal-to-background ratio as much as possible, an optimal particle detection efficiency is needed for the Veto-2 system. Therefore, the detection efficiency was measured using four scintillator-SiPM tiles stacked vertically. Since high-energy particles are needed to pass through all four plastic scintillators, cosmic rays were used to irradiate the detectors. The pulse height spectra of all four units were measured on the condition of a coincidence in signals between the detector at the top and the bottom of the stack. In this way, the abundance of signals in the two units layered in the middle was determined to obtain the detection efficiency of the middle detectors [27]. A schematic drawing of the DAQ system is shown in figure 22. The pulses from the SiPMs are first amplified by the 12-channel amplification board. For the creation of the gate for the Analogue-to-Digital-Converter (ADC), the digital ToT signals of the outermost SiPMs were used. Since the logic units require Nuclear Instrumentation Module (NIM) signals and the ADC requires single-ended voltage pulses, a converter was used to transform the LVDS and analogue differential signal (DS) to single-ended signals each. To elongate the gate in order to include the analogue peaks, a delay trigger was installed. The ADC used was a 32-channel 12-bit peak-sensing Versa Module Eurocard Bus (VMEbus)-ADC of the type CAEN V785.

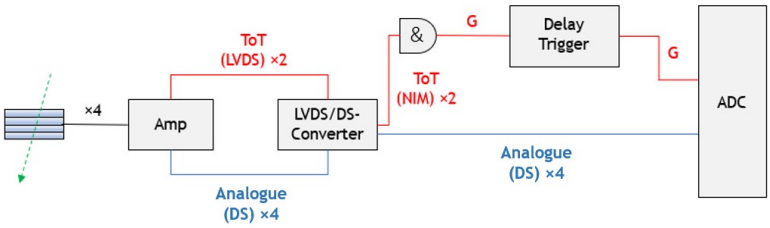

Figure 22: Schematic drawing of the circuit connecting the stacked detectors (left) to the amplification board (Amp) and the DAQ (ADC) as well as the logic creating the gate (G).

From now on, the SiPMs will be named SiPM 1 to SiPM 4, starting from the detector at the top and passing through the stack downwards. To obtain better statistics with the relatively low rate of cosmic rays hitting the stack of detectors, data was acquired over the course of four days. Figure 23 shows the obtained pulse height spectra for SiPMs 1 to 4. A threshold of 400 mV was

chosen for the two outer detectors for the suppression of possible low-energetic background and cosmic rays passing the stack diagonally, depositing only a fraction of charge in these scintillators compared to SiPM 2 and SiPM 3 [27].

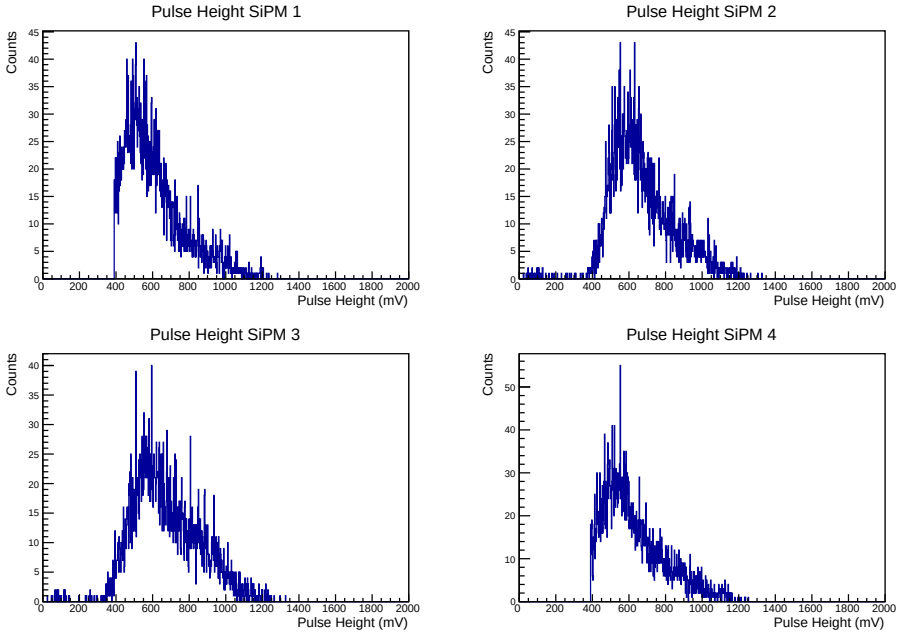

Figure 23: Pulse height spectra observed for the four detectors on the condition of a coincidence between the outermost SiPMs 1 and 4. A threshold for these SiPMs was set at 400 mV. *Picture taken from* [27].

For control, an MC simulation of a spectrum originating from cosmic rays for a scintillator positioned in the middle of the stack was calculated, taking into account muons with normally distributed momenta ranging from 150 to 700 MeV/c [34]. Figure 24(a) shows the simulated muon spectrum (red) as well as the spectrum obtained for SiPM 2. For higher energies (800 to 1500 keV), the simulation is in good agreement with the measured data; for energies between 650 and 700 keV, however, the calculation does not provide an accurate description of the measured cosmic ray data. This can be explained by the rather simple nature of the MC simulation, which does not include low-energy contributions to the background [27].
In the final setup at the SIDDHARTA-2 experiment, the Veto-2 will not be exposed to cosmics as the main source of background but rather to the decay products of the K^-N-reaction. Therefore, another MC simulation was performed for the comparison of the cosmic ray spectrum to the spectrum resulting from the expected DAΦNE background environment, including $\Sigma^{\pm}\pi^{\mp}$, $\Sigma^0\pi^0$, $\Lambda\pi^-$, $\Sigma^0\pi^-$ and $\Sigma^-\pi^0$. Eventually, in the decay of these reaction products, charged pions, protons, neutrons and gammas are produced which constitute the main background source surrounding the Veto-2 system [34]. The spectrum calculated in this way is shown in figure 24(b).

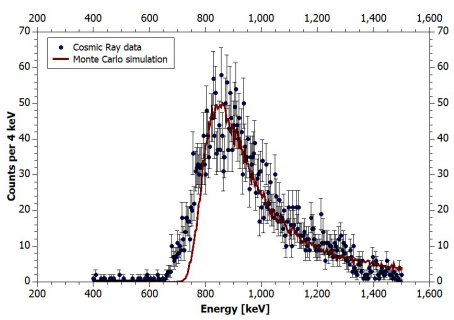

(a) Observed cosmic ray data for SiPM 2 with MC simulated spectrum expected for muons (red). *Picture taken from* [27].

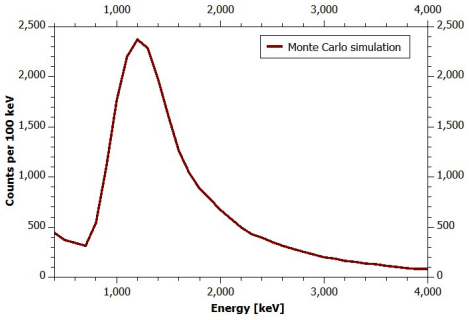

(b) MC simulation of the energy spectrum expected from realistic background (K^-N reaction products) at SIDDHARTA-2. *Picture taken from* [27].

Figure 24: Measured and simulated cosmic ray data compared to spectrum expected with the background at DAΦNE.

When comparing the observed spectra with the simulated spectrum for the realistic background at SIDDHARTA-2, the shape of the spectra is very similar. Despite this, the spectrum for the K^-N-background is slightly shifted towards higher energies with the peak maximum for the calculated spectrum positioned between 1200 and 1400 keV, which differs from the observed cosmic ray peak position by approximately 300 to 500 keV. This effect originates from a higher energy loss of the decay products in the scintillators compared to cosmic rays. However, there is no indication for this spectral shift to have any impact on the detection efficiency [27].

For the determination of the detection efficiency, only signals above a threshold of 300 mV in the SiPMs in the middle of the stack, SiPM 2 and SiPM 3, were included in the calculation. This threshold was high enough to consider only cosmic ray events, while simultaneously compensating for the possibility of the scintillator tiles not being accurately allineated, since the threshold for the outer detectors was set higher at 400 mV. Thus, the detection efficiencies observed for SiPM 2 and SiPM 3 were $(99.05 \pm 0.14)\%$ and $(99.14 \pm 0.14)\%$, respectively [27].

Figure 25 shows the multiplicity of the detectors' response. The bins on the x-axis correspond to the number of SiPMs with a signal above a certain threshold for the inner and outer detectors each. As for the determination of the efficiency, a threshold of 400 mV was set for the outer detectors and a threshold of 300 mV for the two detectors in the middle.
In approximately $(98.8 \pm 0.2)\%$ of cases, in all four detectors a signal above threshold was detected. In $(0.55 \pm 0.13)\%$ of cases, only three units registered a cosmic ray hit and in $(0.67 \pm 0.13)\%$, only two detectors observed an event,

corresponding to the top and bottom units due to the required coincidence. These events can be explained by the possibility of the detectors not being stacked perfectly aligned.
In summary, the detection efficiency of the Veto-2 system was found to be very high with $\sim 99\%$, as was expected.

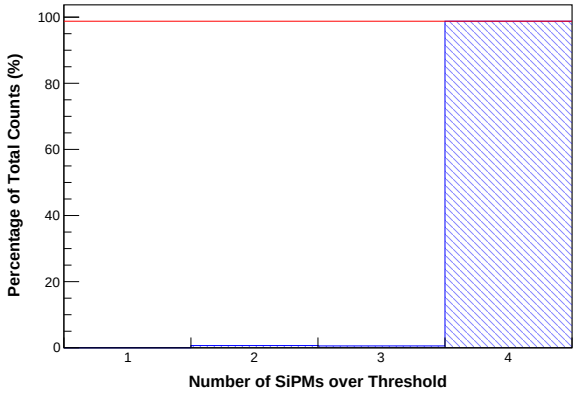

Figure 25: Multiplicity of signals detected in the detector stack. In over 98% of cases, in all four detectors an event above threshold was registered.

5.4 I-V-Curves

In August 2018, the veto counters were planned to be tested under more realistic conditions using a pion beam with a pion momentum of approximately 200 MeV/c at the Paul Scherrer Institute (PSI) in Switzerland. A parasitic setup developed for the measurement of the beam width and position is shown in figure 26(a). Furthermore, the detection efficiency was planned to be determined again, this time using negatively charged pions as source instead of cosmic rays which were used in the previous measurement performed at SMI. Due to radiation safety measures, a concrete bunker was built surrounding the entire setup. This housing, in combination with the high outside temperatures and the heat radiated off by the setup, resulted in an increase of temperature inside the bunker to around 40°C. The bunker is shown in figure 26(b).

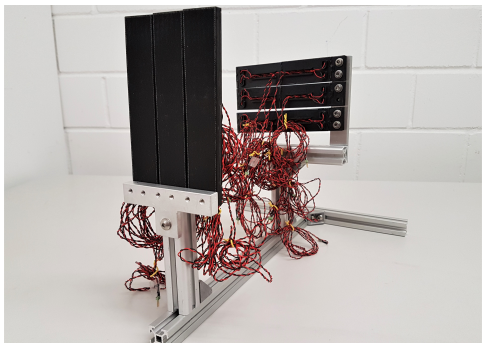

(a) Detector configuration planned for the measurement of the beam position and width at PSI.

(b) Outside view of the concrete bunker surrounding the setup at PSI for radiation safety.

Figure 26: Experimental setup at the pion beam area at PSI.

In the beginning, the scintillator-SiPM units were used for the tuning of the pion beam. During this process, a sudden flash of positively charged pions (π^+) with a rate of approximately 10^9 Hz briefly hit the detectors, leading to the SiPMs being completely saturated and blind to any further particle hits for several seconds. After this event, the pulse heights obtained with these SiPMs were significantly lower than usual for the same bias voltage (see figure 27). Since the detectors did not operate properly any more, the planned measurements could not be performed at PSI.

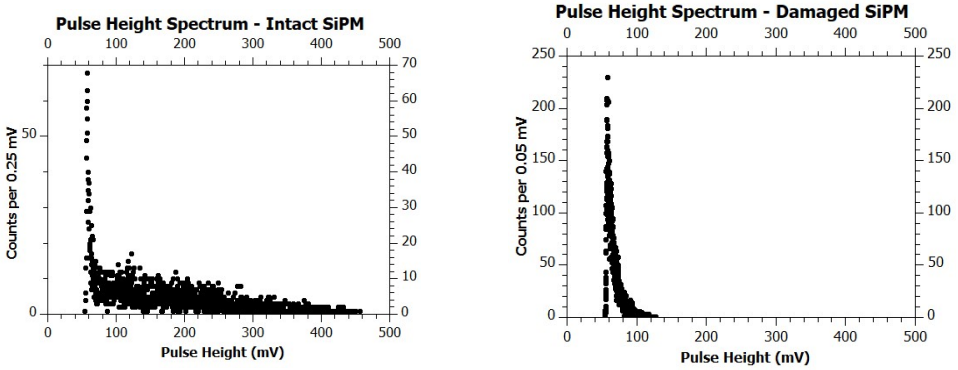

(a) Pulse height spectrum observed for an intact SiPM with Sr-90 source. Pulses up to a height of approximately 450 mV were observed.

(b) Pulse height spectrum observed for a presumably damaged SiPM from PSI with Sr-90. The maximum pulse height is only approximately 125 mV.

Figure 27: Comparison of pulse height spectra for an intact SiPM and a SiPM exposed to the π^+ at PSI.

To confirm that the detectors indeed had been damaged during this event, I-V-curves were obtained for eight intact SiPMs and eight SiPMs exposed to the π^+ at PSI. For this measurement, the board shown in figure 28 was used to apply the bias voltage to each diode.

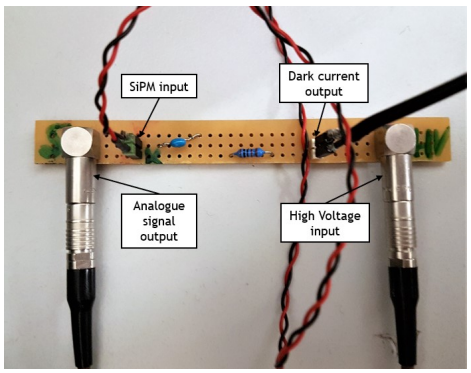

Figure 28: Board used to bias the SiPM and measure the dark current.

The bias voltage was increased up to 32 V for each intact and up to 29.5 V for each presumably damaged SiPM, and the resulting leakage current was measured. The observed curves for the intact SiPMs and supposedly damaged SiPMs are shown in figure 29(a) and (b), respectively.

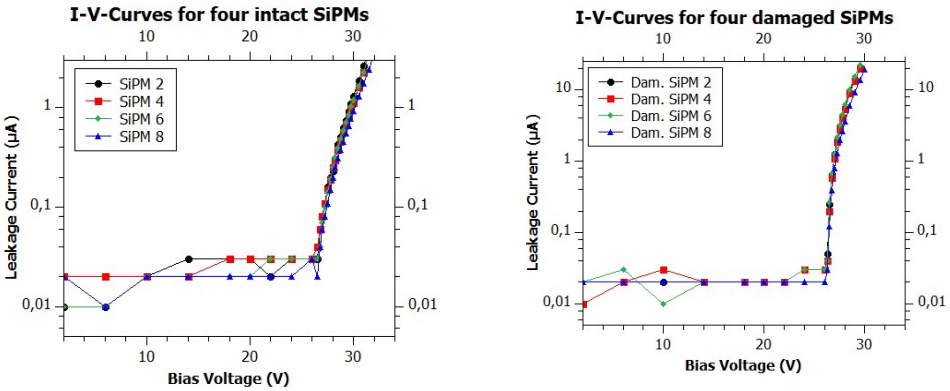

(a) Observed I-V-curves for four intact SiPMs.

(b) Observed I-V-curves for four SiPMs damaged at PSI.

Figure 29: I-V curves obtained for four intact and four damaged SiPMs.

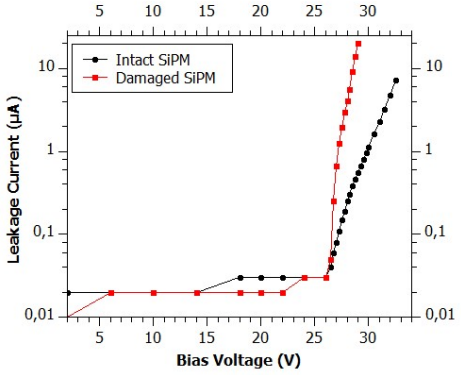

Figure 30: Direct comparison of I-V-curves for one damaged (red) and one intact (black) SiPM.

Figure 29 clearly shows a difference between the observed I-V-curves for intact SiPMs and the SiPMs damaged at PSI. The leakage current for the damaged SiPMs increases much faster for a bias voltage above the breakdown voltage than for properly functioning SiPMs; for a bias voltage of 29 V, the dark current flowing through a damaged SiPM was already around 12.7 μA, whereas for an undamaged diode the dark current was at approximately 0.6 μA. This effect can be seen more clearly in figure 30, where an example of I-V-curves for one intact and one impaired SiPM are displayed.
Additionally, the breakdown voltage was influenced by the impairment of the detectors as well. On average, the breakdown voltage for the harmed SiPMs was (26.3 ± 0.2) V, while for the functional ones it was (26.6 ± 0.2) V, as can be seen in figure 31.
To sum up, the damage to the SiPMs was not yet fully understood up until

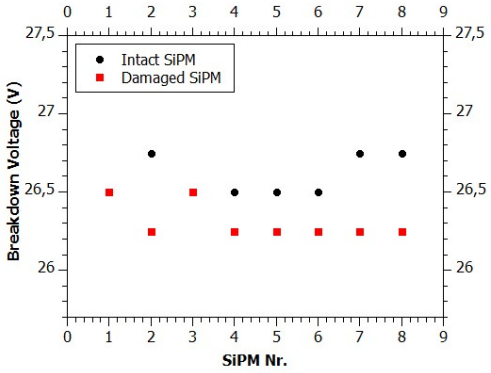

Figure 31: Comparison of the breakdown voltages for different damaged (red) and intact (black) SiPMs.

the end of this Master's thesis. Since high temperatures alone could be excluded as the main source for the impairment (see chapter 5.5), it was assumed that a combination of the high temperature environment with the high rate flash of pions hitting the detectors likely caused the damage. Due to these circumstances, the dark count rate of the diodes, which is highly temperature dependent, was increased significantly. This, combined with the π^+ flash, might have resulted in a very high current flowing through the detectors, possibly burning some of the quenching resistors in the microcells. This partial damage of the microcells could explain the steep increase and noteworthy variation in leakage current above the breakdown voltage on the one hand as well as the considerably lower pulse heights for equal dark current on the other hand.
Therefore, studies regarding the radiation hardness of the SiPMs would be of interest; due to time constraints, however, this was not possible within the scope of this Master's thesis. In addition, during the SIDDHARTA-2 experiment, the Veto-2 system will not be exposed to such high rates or surrounding temperatures; hence, a damaging of the SiPMs in this way is not expected.

5.5 Temperature Studies

The temperature dependent behaviour of the detectors as well as the electronics is of interest not only due to the damage that occurred to the SiPMs at PSI, but also because the Veto-2 system will be operated at approximately −10°C during the SIDDHARTA-2 experiment. Therefore, the performance of the veto units and the amplification boards was studied separately in a climate chamber of the type Vötsch VT 7021.

5.5.1 Temperature Studies of the Amplification Boards

Initially, the amplification boards were installed inside the climate chamber. Since a broad temperature range was tested, measures to avoid condensation and humidification of the electronics had to be taken. Therefore, the amplification board was placed on top of a small table to avoid direct contact of the board with the walls of the chamber (see figure 32). Additionally, a compressor was installed to flush the chamber volume with dry air during temperature changes.

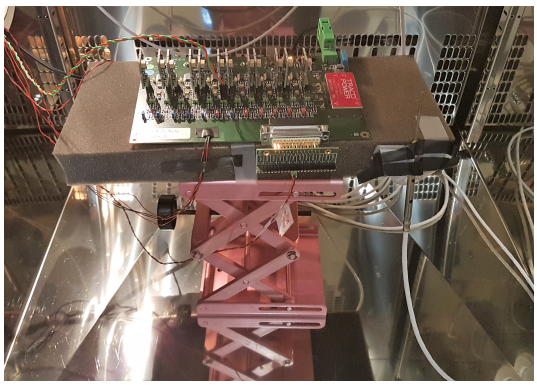

Figure 32: Amplification board set up in the climate chamber to study its temperature dependent performance.

The scintillator-SiPM unit was placed outside of the climate chamber in a blackbox and was kept at a constant temperature of 25°C, which was surveilled with a PT1000 temperature sensor inside the blackbox and logged over the course of each measurement with a Picotest PT-104 PT100 Data Logger. An additional PT100 was mounted directly on the amplification board inside the climate chamber; its temperature was logged with the Picotest monitor as well.
A Na-22 source was placed inside the blackbox with the detectors and the pulse height spectra were measured using the oscilloscope for four different temperatures of the amplification board. Since the boards will be mounted outside of the vacuum chamber at the final setup for SIDDHARTA-2 and will thus not be cooler than room temperature, the pulse height measurements were performed at 10°C, 20°C, 30°C and 40°C. To further avoid any condensation inside the setup, the transitions between different temperature points were performed

slowly and in steps of 5°C.
For each temperature, data was acquired for approximately six hours. As described before, a temperature sensor was placed with the detector to monitor its temperature. Figure 33 shows an example of one of these temperature curves during a measurement. The pink curve corresponds to the PT1000 sensor placed with the detectors outside of the climate chamber, while the blue curve describes the temperature of the electronics inside. Due to the heat produced by the board itself, its temperature was slightly higher than the surrounding temperature inside the chamber. As can be clearly seen, the temperature of the scintillator-SiPM unit was constant, with the strongest fluctuations being in the order of 0.5°C, as was the case during all performed measurements.

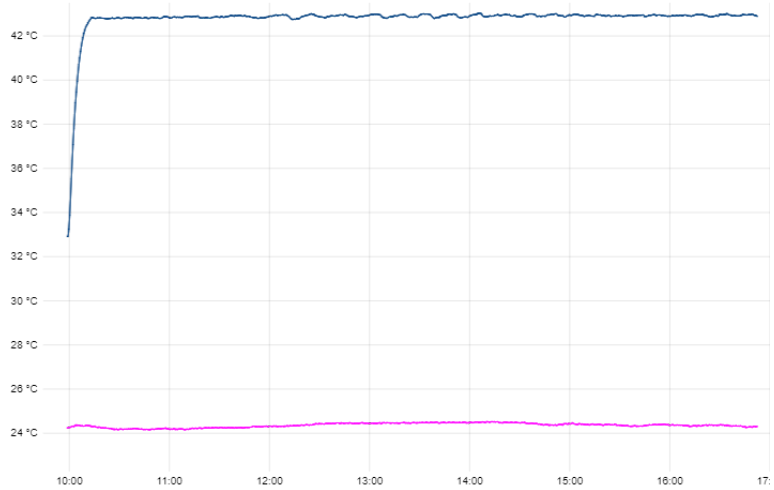

Figure 33: Temperature curves monitored during the measurement at a temperature of 40°C. The pink curve corresponds to the detector outside of the climate chamber. The temperature of the amplification board is shown in blue.

The pulse height spectra obtained in this way are shown in figure 34. All of these spectra clearly show two Compton edges at different pulse heights corresponding to different energies deposited in the scintillators. Due to the detector configuration, only the gamma rays emitted by Na-22 were observed with energies of 511 keV and 1275 keV, resulting in the two Compton edges. The pulse height position of these edges was analysed to compare the behaviour of the electronics at the four different temperatures. In order to do so, the position of the Compton edges was determined by first smoothing the data by calculating a floating average of 50 data points. This was necessary due to a pick-up noise structure in the pulse height spectra, as shown in figure 35(a). After the smoothing of the data, the pulse height position corresponding to the horizontal middle of the edge was calculated for both edges at each temperature. One spectrum with the smoothed edge data is shown in figure 35(b).

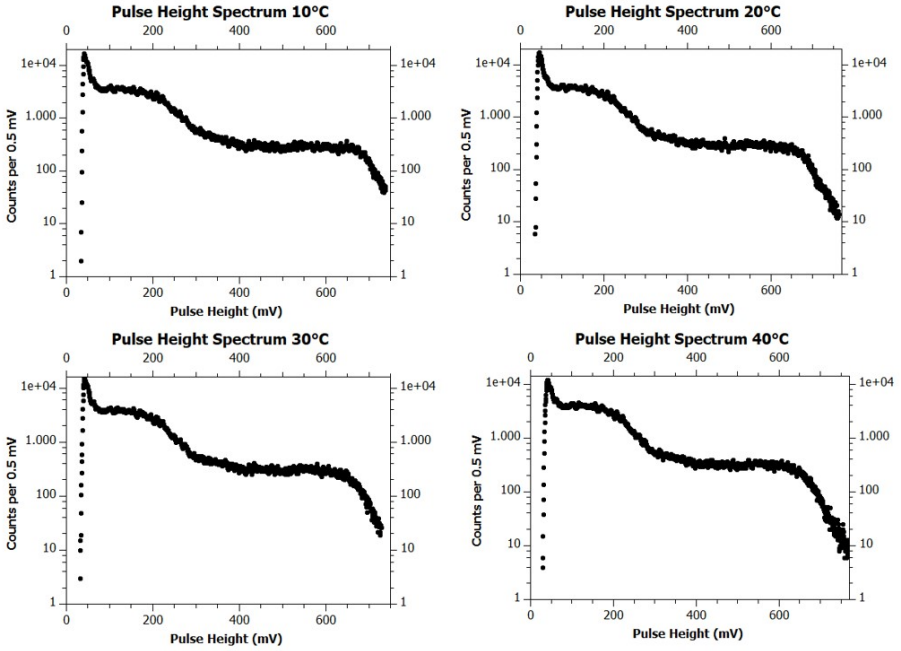

Figure 34: Pulse height spectra observed with the amplification board operated at different temperatures.

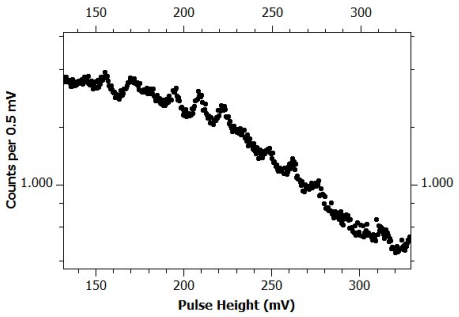

(a) Observed noise structure in the pulse height spectrum at 10°C in the region of the first Compton edge.

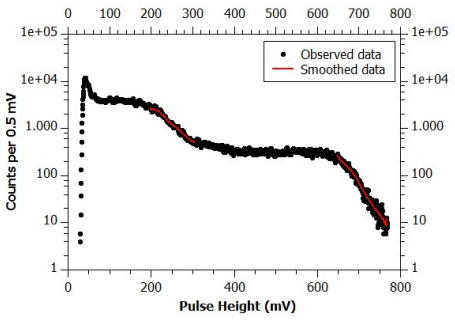

(b) Pulse height spectrum at 40°C with floating average smoothed data at the Compton edges (red).

Figure 35: Noise structure in the pulse height spectra necessitating a smoothing of the data to determine the position of the Compton edges.

Figures 36 and 37 show the positions of the first and second Compton edge, respectively, plotted against the temperatures of the amplification board. The error bars correspond to the propagated standard error of the floating average.

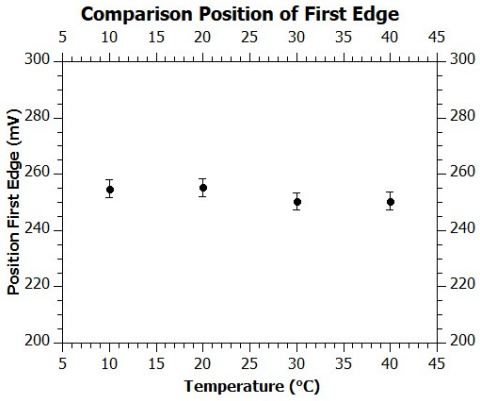

Figure 36: Pulse height position of the lower-energetic Compton edge correlated to the temperature of the amplification board.

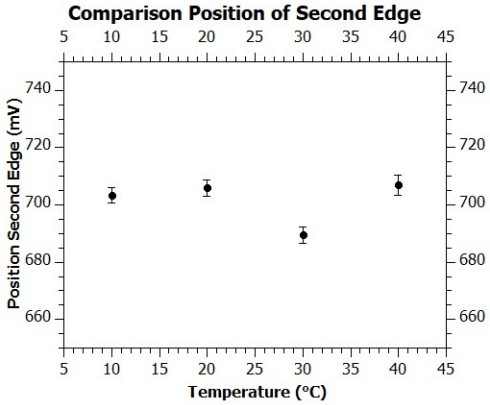

Figure 37: Pulse height position of the second, higher-energetic Compton edge in relation to the temperature of the amplification board.

In both cases, the position of the edges does not shift considerably depending on the temperature of the amplification board. A slight variation could have been introduced by the smoothing of the data or the choice of range around the Compton edges within which the data was smoothed. In general, however, it can be concluded that the amplification board operates very stably at a multitude of temperatures. At SIDDHARTA-2, the amplification boards are expected to operate within the temperature range tested during this measurement. Due to time constraints, not every one of the twelve boards could be tested. Despite this, all of the boards are expected to operate very similarly. Hence, for SIDDHARTA-2, no temperature-dependent behaviour of the electronics of the Veto-2 system is expected.

5.5.2 Temperature Studies of the Veto-2 Detector Units

Of even greater importance for the final configuration of the Veto-2 system was the observation of the temperature behaviour of the detector units, i.e. the scintillators and SiPMs. Hence, their performance was studied by placing them inside the climate chamber with a Na-22 source. A detector box was placed on a small table like the amplification boards and wrapped in black, light-tight fleece (figure 38). The amplification board was set up outside of the climate chamber and kept at a constant temperature to obtain a measurement independent of the electronics' temperature.

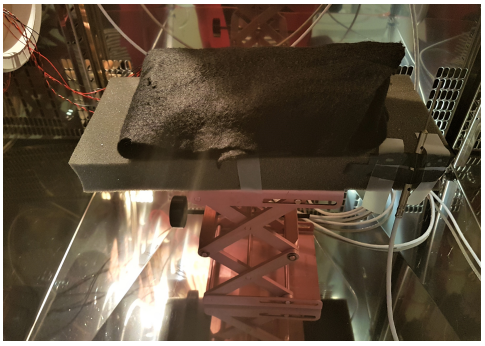

Figure 38: Detector box wrapped in light-tight fleece inside the climate chamber to study the temperature dependence of the detector's performance.

Again, the pulse height spectra were measured with the oscilloscope for temperatures of the SiPMs between −40°C to 40°C with steps of 10°C. As for the measurement on the amplification boards, the temperature of the detector and the electronics was monitored by fixing a PT100 and PT1000 temperature sensor on the detector box and the amplification board, respectively. Their temperature was measured using a Picotest temperature logger. Also, the chamber was again flushed with dry air to avoid any humidification of the setup. Additionally, the transitions between temperatures were performed slowly and in steps of 5°C, as in the previous measurement.
For each temperature, data was acquired for 60 min. Furthermore, a background measurement without source was performed for temperatures of 0°C and 20°C to compare with the Na-22 spectra. The pulse height spectra obtained with the Na-22 source are shown in figures 39 and 40.
A first notable observation in the spectra was their shifting to a higher pulse height range with decreasing temperature. When comparing the spectrum for a temperature of 40°C with the spectrum for −40°C, the maximum observed pulse height increased from approximately 500 mV to 790 mV. Moreover, over the course of the measurements it was observed that for temperatures below 20°C, the dark current of the SiPMs, i.e. their bias voltage, had to be reduced in order to obtain their entire pulse height spectrum. This effect was the result of the amplification boards reaching saturation at pulse heights around 800 mV. It can clearly be seen e.g. in the spectra measured at −10°C and

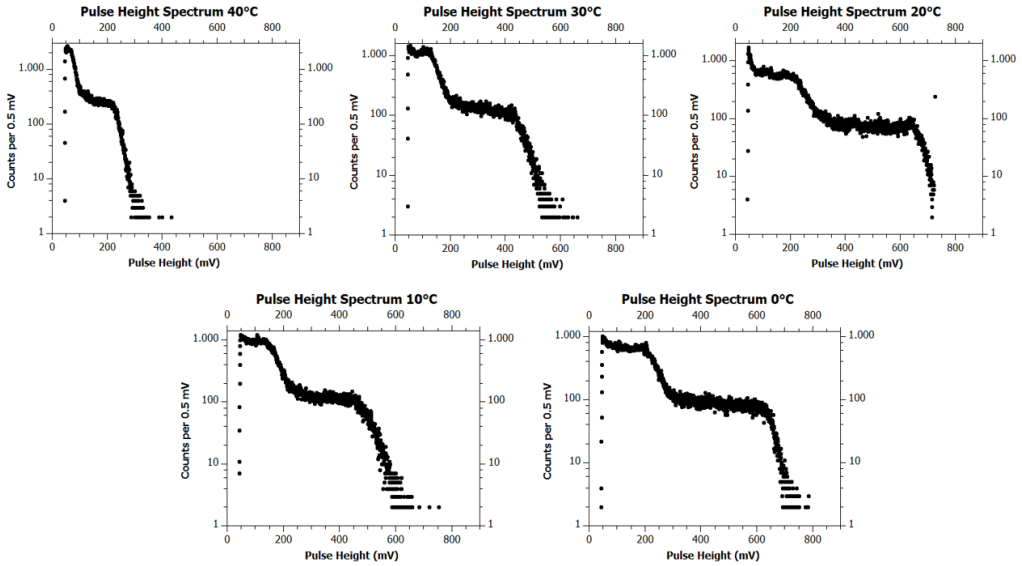

Figure 39: Observed Na-22 pulse height spectra for temperatures of the detector between 0°C and 40°C.

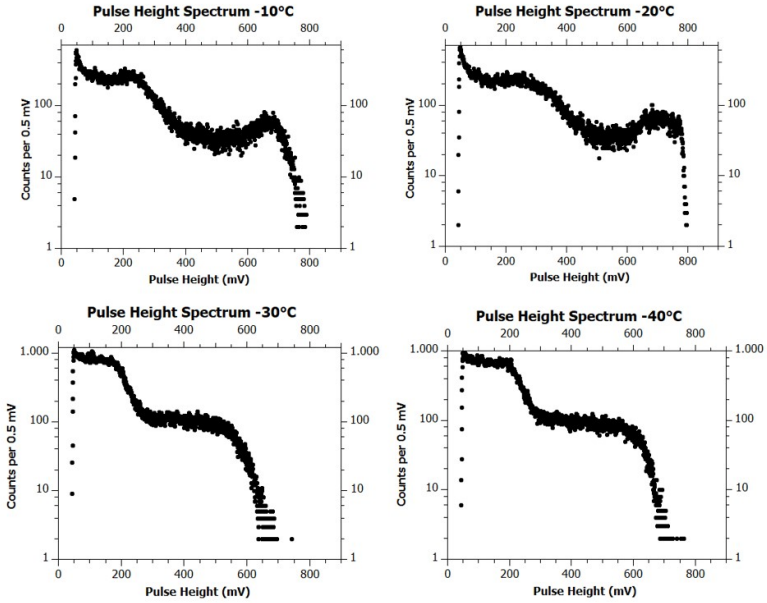

Figure 40: Observed Na-22 pulse height spectra for temperatures of the detector between −10°C and −40°C.

−20°C in figure 40, where at the position of the second Compton edge a heightened, peak-like structure appeared where the pulse heights above the saturation point of the amplification boards were summed up. Hence, the dark current was adjusted from 3.3 μA in the range of 40°C to 20°C to 1 μA for 10°C to −20°C, and eventually to 0.65 μA for −30°C and −40°C.

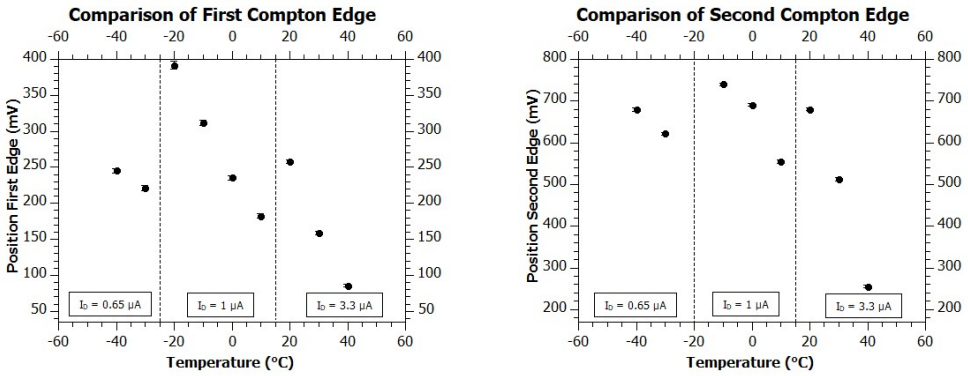

(a) Pulse height positions of the lower-energetic Compton edge for different SiPM temperatures.

(b) Pulse height positions of the Compton edge at higher energies for varying SiPM temperatures.

Figure 41: Comparison of the pulse height positions of the two observed Compton edges for each temperature.

As done for the temperature studies regarding the amplification boards, the pulse height positions of the Compton edges in the spectra were used to compare the different temperature points. This evaluation is shown in figure 41(a) and (b) and was performed in the same way as described in 5.5.1. The change of the dark current for certain temperature ranges is indicated in the graphic as well. The position of the second Compton edge at −20°C was not included in the final analysis due to the amplification board operating nearly saturated, leading to an accumulation of data in this range.
For both edges, the non-linear relation between the position of the Compton edge and the detector's temperature results from the necessary variation of the bias voltage, i.e. the variation of the gain. The error bars correspond again to the Gaussian propagated standard error of the floating average calculated for packages of 50 data points. Apart from the variations due to the changing gain, the data points, like the raw pulse height spectra, show a shift of the Compton edges to higher pulse heights for decreasing temperatures.

This effect probably results from a combination of contributing factors and its explanation is non-trivial. Although Scionix Holland specifies the light output of the scintillators as nearly temperature independent within a range of −60°C to 60°C [32], a small temperature dependence cannot be excluded in this measurement. In addition, multiple parameters of the SiPM are known to be temperature dependent [31]. Figure 42(a) (taken from [31]) shows that

the quenching resistance significantly increases for decreasing temperatures in AdvanSiD-SiPMs.

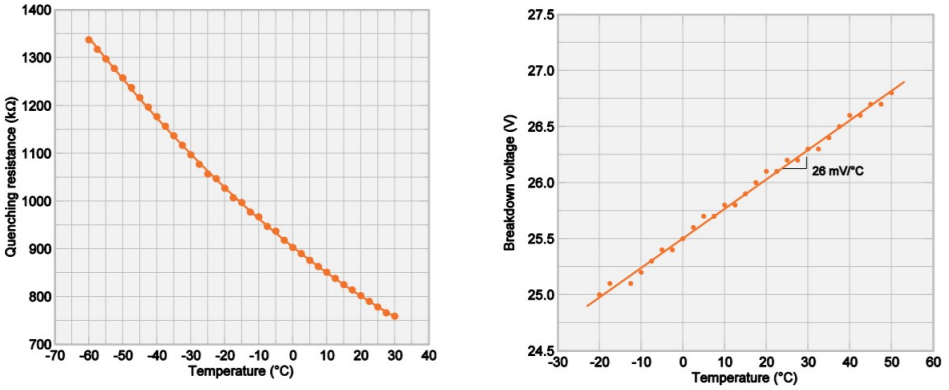

(a) Quenching resistance in relation to the SiPM temperature. *Picture taken from* [31].

(b) Temperature dependence of the breakdown voltage of the AdvanSiD-SiPMs. *Picture taken from* [31].

Figure 42: Temperature dependence of the SiPM properties like quenching resistance and breakdown voltage.

For a constant dark current in the SiPM, this would result in higher output pulses for lower temperatures. However, it cannot be assumed that the dark current is constant under temperature variations; this was observed by measuring the leakage current at different temperature points of the SiPMs. This behaviour is related to the temperature dependence of the breakdown voltage of the diodes, resulting in a temperature dependence of the overvoltage (see figure 42(b), taken from [31]). To quantify this effect, the I-V-curves of the SiPM in the climate chamber were measured at −40°C, −30°C, 0°C and 20°C in addition to acquiring the pulse height spectra. For this, instead of the amplification board, the board described in 5.4 was used outside the climate chamber to bias the SiPM and the dark current was measured using an amperemeter. The curves obtained are shown in figure 43.
While for overvoltages around 2 V and higher the slope of the I-V-curves is very similar for all temperatures, a temperature dependence of the breakdown voltage is indicated. In comparison to the breakdown voltage of the diode at −40°C, the bias voltage at 20°C has to be approximately 0.5 V higher for the breakdown to occur. The datasheet of the SiPMs lists a linear dependence of the breakdown voltage with a temperature coefficient of 26 mV/°C, as shown in figure 42(b).
A behaviour as extreme as described in the datasheet was not observed here, as a temperature coefficient of 26 mV/°C corresponds to a difference in breakdown voltage from −40°C to 20°C of 1.56 V, which is approximately larger by a factor of three than the difference measured in the climate chamber. However, the properties described in the datasheet generally confirm the observed temperature dependent behaviour of the breakdown voltage. This effect will

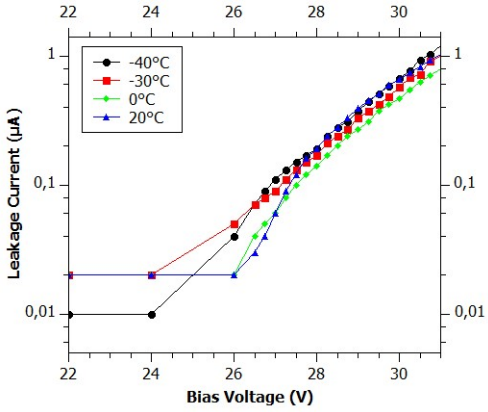

Figure 43: Comparison of the I-V-curves observed at four different temperatures of the detectors.

have to be taken into consideration in terms of the final configuration of the electronics at SIDDHARTA-2.

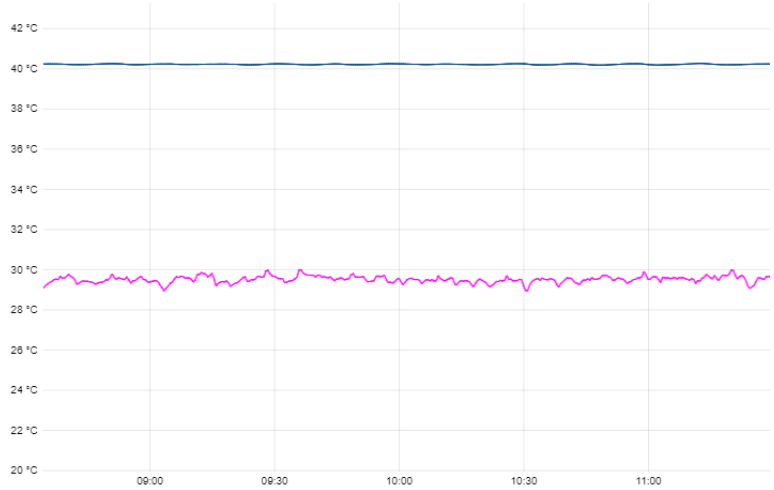

Figure 44: Example temperature curves during the 40°C measurement. The blue curve corresponds to the detectors inside the vacuum chamber, the pink curve shows the temperature of the electronics outside.

It can be excluded that these observations were influenced by temperature fluctuations of the electronics. Firstly, the temperature of the board was monitored (see figure 44) and found to be constant over the course of the measurements with maximum fluctuations in the order of 1°C. Secondly, the amplification board operates stably at various temperatures, as described before, so these small fluctuations would not influence the performance of the electronics.
The background spectrum measured at 0°C is shown in figure 45. The pulse heights observed without source in general are below 150 mV and do not exceed approximately 210 mV. These few higher pulses probably originate from

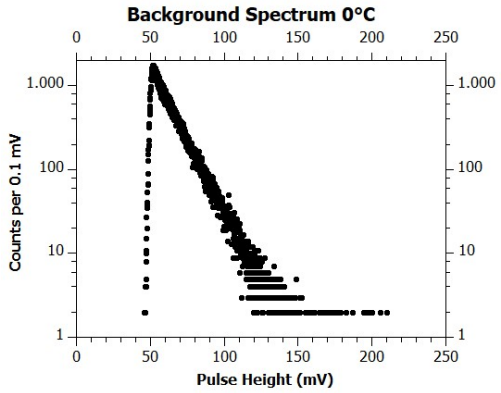

Figure 45: Background spectrum without Na-22 source measured for a detector temperature of 0°C .

cosmic rays hitting the detectors, which cannot be avoided neither in this measurement nor at SIDDHARTA-2. Since the average pulse heights in the background measurement without source are much smaller than the position of the lower-energetic Compton edge observed with Na-22, which for 0°C is between approximately 200 mV to 300 mV, the background contribution to the final spectra used for the analysis is negligible. A background subtraction was not needed in the analysis.

Overall, the shifting of the spectra to higher pulse heights for lower temperatures, although not trivially, can be understood as a sum of multiple contributing effects in the SiPMs. An influence of the scintillators' light output cannot be excluded. The combination of the temperature dependence of the quenching resistance and the breakdown voltage results in a temperature dependent behaviour of the gain of the SiPM, which eventually leads to the output current being temperature dependent.
For a more complete characterisation of the observed behaviour, the performance of the SiPMs alone, without scintillators, would have to be studied at different temperature points. This would allow for the decoupling of effects originating from the scintillators and lead to a better understanding of the SiPM properties.

5.6 Simultaneous Read-Out of Multiple Veto-2 Detectors

In order to determine the proper adjustments of the electronic settings regarding the values for the gain and threshold on the amplification boards for the DAQ, a test to read out twenty channels simultaneously was performed. In order to do so, two of the twelve-channel amplification boards were used to amplify the signals of twenty SiPMs and four additional SiPMs attached to a large scintillator bar, out of whose signals the gate for the VME TDC (CAEN V1190A Mutlihit TDC) was created. The ToT spectra were measured for all twenty detectors.

The twenty SiPMs of the Veto-2 system were placed side by side on top of the longer scintillator bar and irradiated with cosmic rays. On each side of the large scintillator a total of four SiPMs was attached, with two SiPMs connected in series, resulting in two pairs of SiPMs per side. Coincidences in ToT signals of the two pairs per side were built and in turn connected with each other to significantly reduce the dark count rate. This final coincidence acted as a trigger signal for the TDC.
Since the SiPMs slightly vary with respect to their internal gain and pulse height range, the gain for the SiPMs was adjusted to ensure very similar pulse height spectra for all detectors. The threshold for the ToT signals was set in a way to obtain a digital signal at approximately the same pulse height for each SiPM.
The ToT spectra observed are shown in figures 46 and 47. All spectra were obtained simultaneously by reading out two twelve-channel amplification boards. The first four channels of Board 1 were needed for the four pairs of SiPMs on the scintillator bar used for the creation of the trigger and are not shown in figure 46. The spectra for all twenty SiPMs show that for the chosen threshold and gain settings the ToT for all SiPMs is approximately 200 to 300 ns.

To sum up, this test was crucial for a better understanding of the mutual influence of the read-out settings on each other as well as on the obtained ToT spectra. The knowledge gained during this measurement, in particular the influence of the gain settings on gain variations in the ToT spectra, is of great value for the final preparation and configuration of the electronics in the final SIDDHARTA-2 setup.

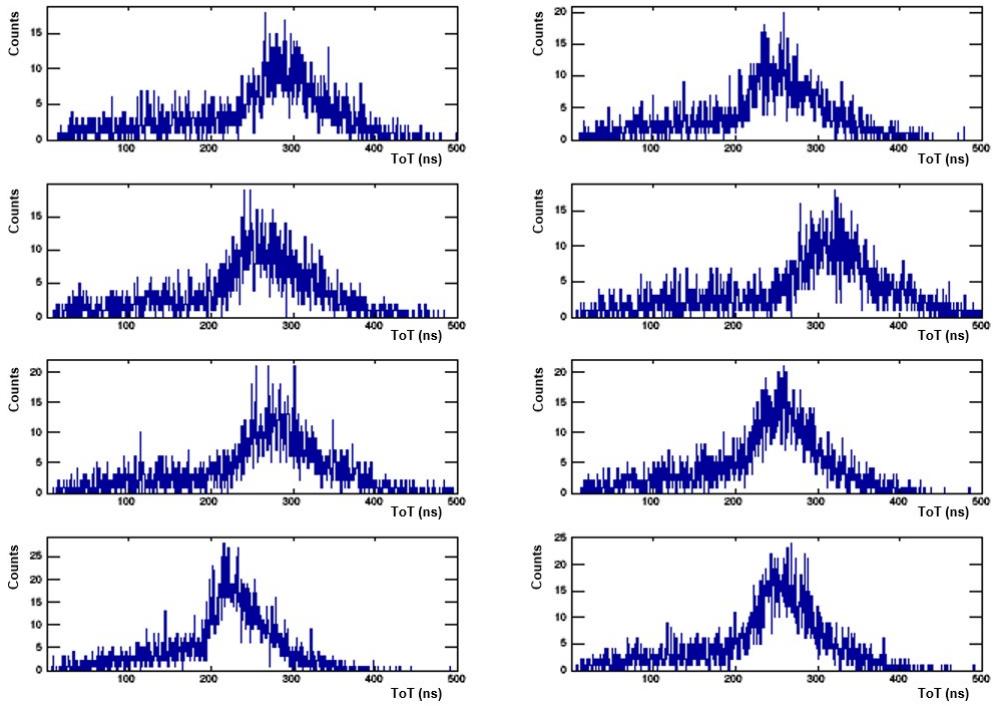

Figure 46: ToT spectra resulting from eight Veto-2 detectors read out simultaneously with the first amplification board.

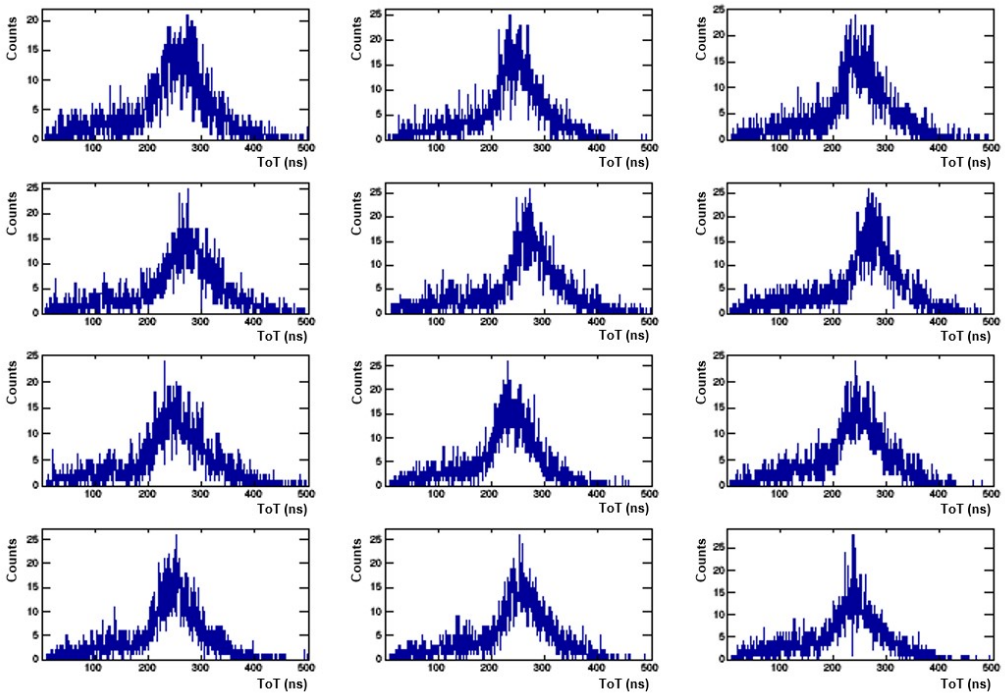

Figure 47: Remaining twelve ToT spectra obtained simultaneously read out with the second amplification board.

5.7 Correlation of ToT and Amplitude

Since for the DAQ of the Veto-2 system only a TDC will be used and therefore only the ToT signals will be recorded, the correlation of the width of the ToT signal and the amplitude of the analogue SiPM pulse is of interest. Thus, the relation between the two signals was determined. Due to the nature of the ToT signal, it can be expected that gates with a greater width correspond to higher analogue pulses and vice versa.

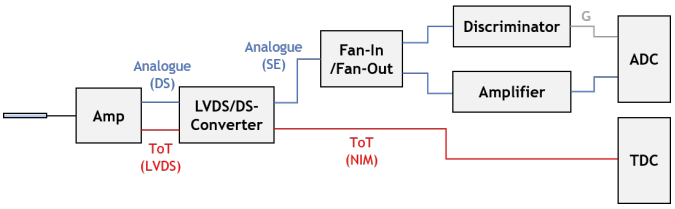

Figure 48: Schematic circuit for measuring the correlation between the SiPM amplitude and the ToT width. The gate (G) was created from the analogue signal (blue), the NIM ToT signal is shown in red.

A Sr-90 source was placed on top of the detector unit to increase the rate and thus obtain higher statistics. For the amplification of the SiPM signals, a twelve-channel amplification board was used. The pulse height spectrum and ToT spectrum were acquired with a 12-bit peak sensing VME ADC (CAEN V785) and a VME TDC (CAEN V1290N). This TDC requires NIM inputs, thus a converter to tranform the LVDS signals to NIM standard was needed. Since the ADC can cover a pulse height range up to 4 V [35], an additional amplifier (CAEN 16 Channel Spectroscopy Amplifier, gain ~ 3.5) was used for the analogue SiPM pulses. A schematic drawing of this circuit and the DAQ is shown in figure 48. The gate (G) required by the DAQ as a trigger signal was created from the discriminated analogue signal with a threshold of approximately 80 mV.

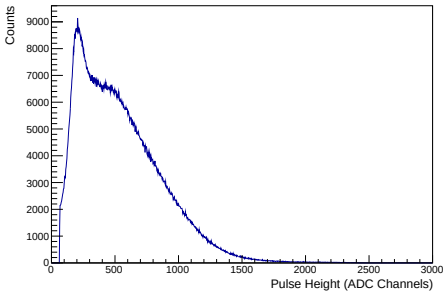

(a) Pulse height spectrum observed with a Sr-90 source.

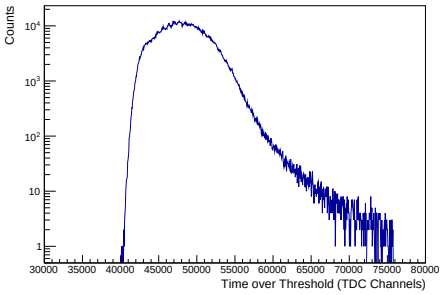

(b) Observed ToT spectrum in units of TDC channels.

Figure 49: Pulse height and ToT spectra acquired using a Sr-90 source.

Figure 49 shows the obtained pulse height and ToT spectra, with the x-axes in units of ADC and TDC channels, respectively. The observed spectra both reflect the expected behaviour. Since Sr-90 is a β-emitter and decays to Y-90, which undergoes β^--decay itself, the pulse height spectrum shows the typical continuous β spectrum.
The final result, the correlation between the amplitude and corresponding ToT, can be seen in figure 50. For pulse heights between approximately 250 and 1200 ADC channels, the data follows a linear relation. The correlation for lower pulse heights slightly differs from this behaviour, as expected. For low pulse heights, noise has greater impact on the amplitudes. Since the MIPs expected at SIDDHARTA-2 will produce much higher pulses, these fluctuations will not be of concern in the final experiment.

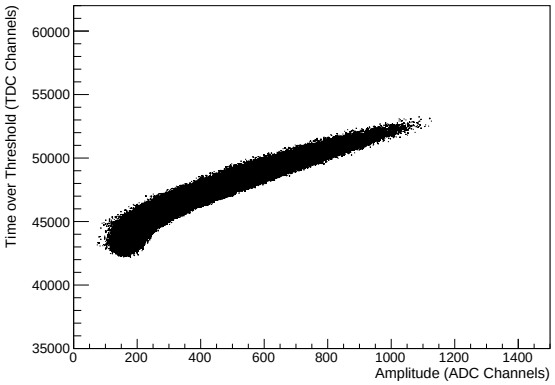

Figure 50: Correlation between the amplitude of the SiPM pulse and its ToT width.

5.8 Vacuum Tests

Since the Veto-2 system consists of boxes which are made of porous material, the possibility of outgassing in a vacuum environment has to be considered. Water vapour and other gasses could adhere to the pores of the plastic and get released when evacuated. Therefore, ten of the veto-counter boxes where placed inside a small vacuum chamber, to check if this was the case (figure 51(a)). This test was performed at room temperature of approximately 24°C.

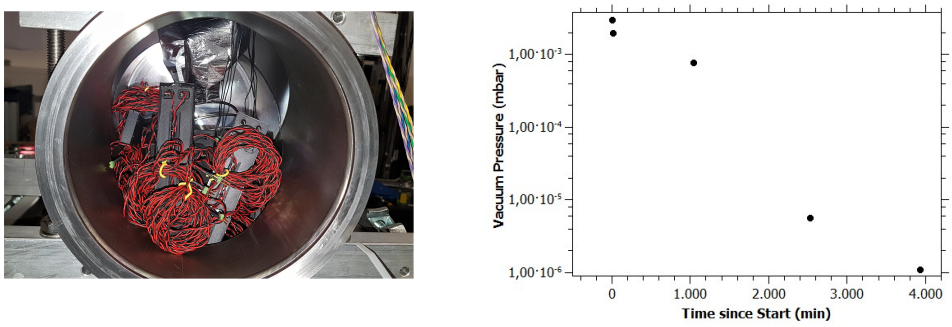

(a) Detector units placed inside the vacuum chamber to check for outgassing and to determine the highest achievable vacuum.

(b) Vacuum pressure during the pumping process. After approximately 1.5 days, the 10^{-6} mbar range was reached.

Figure 51: Setup and pressure curve for a first vacuum test with the Veto-2 detectors.

The forepump, a scroll pump of the type Agilent Technologies IDP-3, was started and followed by an Agilent Technologies TwistTorr 84 FS turbopump. After approximately 2.5 days, a vacuum pressure of 1.1×10^{-6} mbar was reached. This process is shown in figure 51(b).
The relatively long time it took to reach the high vacuum pressure range for such a small vacuum chamber can be mainly attributed to the large surface of the ten detector boxes inside. Furthermore, the veto counters have never been placed in an evacuated environment before, so outgassing was expected to some extent. Despite this, a good vacuum pressure could be reached and it can be concluded that the Veto-2 system is compatible with the high vacuum operation required for the SIDDHARTA-2 experiment.

6 Installation at DAΦNE

6.1 Installation of SIDDHARTA-2

In autumn of 2018, the installation of the general setup of SIDDHARTA-2 started as beam time was scheduled for the beginning of 2019.
The mounting frame supporting the new vacuum chamber was built and the smaller components, including the electronics for the veto system and SDDs, the cooling structures and the target cell as well as all the detectors could be set up.

(a) Cooling structure for the target cell before installation at the setup.

(b) Cold head, cooling line and target cell wrapped in super-insulation.

Figure 52: Target cell cooling system consisting of a helium cryocooler and cooling line before and after installation at the SIDDHARTA-2 setup.

At first, the cooling structure for the target cell was installed. A 2-stage closed-cycle He cryocooler (Oerlikon Leybold Vacuum Coolpower 10MD) is responsible to cool the target cell down to 25 - 30 K. The target cell is connected to the cryocooler via a structure shown in figure 52, which acts as cooling line. For a better heat contact, vacuum grease mixed with copper powder was applied to all connections. Figure 52(a) shows the target cell connected to the cooling line and the cold head at the bottom, figure 52(b) shows this structure after installing it in the SIDDHARTA-2 setup, with the cold head at the very top and the target cell at the bottom. The cooling line was already partly wrapped in superinsulation, which is necessary to reduce thermal radiation from the vacuum chamber at room temperature. Eventually, the entire structure was wrapped in multiple layers of insulation. The target cell was mounted along with the pipe connecting it to the gas supply and a safety valve and was

enveloped in superinsulation as well, to protect the surrounding SDDs from cooling down close to the temperature of the target.
To avoid cooling the target cell itself too far, a heating resistor was mounted on the connecting structure to keep the temperature constant at approximately 30 K.

After installing the target cooling system, mounting structures for the electronics of the SDDs and the strain reliefs for the cables of both SDDs and the Veto-2 were set up around the target cell (see figure 53(a)).

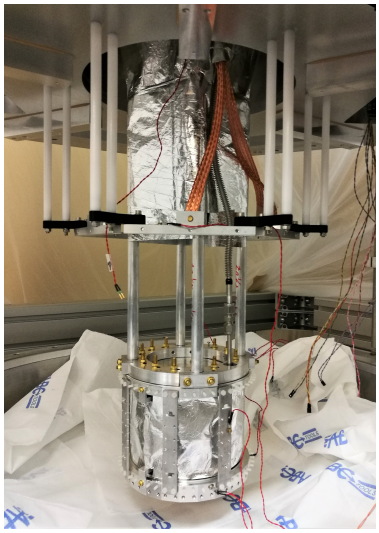

(a) Mounting structure for the strain reliefs and the electronics for the SDDs, connected to the copper cables.

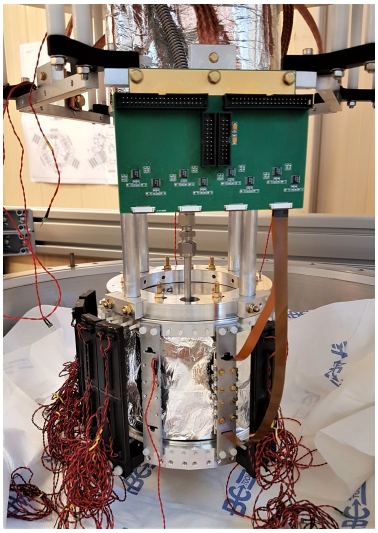

(b) Electronics for the SDDs connecting them with the CryoTigers over the Kapton and copper cables.

Figure 53: Cooling structure for the SDDs and strain reliefs around the target cell.

If additional cooling for the SDDs will be needed, two separate CryoTigers might be used. They were installed at the top part of the setup and wrapped in multiple sheets of superinsulation as well. To connect them to the SDDs, copper cables lead from the CryoTigers to the metal bars holding the electronic boards attached to the Kapton cables from the detectors (figure 53(b)). Each board connects eight SDD arrays with the SDD Front-End Readout ASIC (SFERA) chip outside the vacuum chamber, where ASIC stands for Application Specific Integrated Circuit. The SFERA chip shapes and amplifies the signals and supplies digital signals for the discrimination of certain pulse heights. The SDDs themselves were mounted on aluminium bars around the target cell, which can also be seen in figure 53(b). Since the SDDs must not be cooled down below 100 K, nylon washers and nuts were used to reduce the heat contact between their mounting bars and the target cell. Tests have shown that cooling the SDDs down below 100 K leads to problems with the bonding and

the SDDs even might be detached from their ceramic.

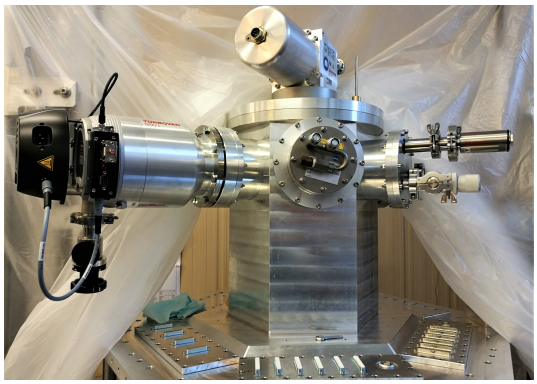

Figure 54: Top part of the SIDDHARTA-2 setup with the cold head, the turbopump, one CryoTiger, safety valves and the feedthroughs installed.

To transport the signals from the SDDs to the DAQ and to provide the HV and low voltage (LV) supply needed to operate the SDDs, high vacuum feedthroughs were necessary. The HV modules and the SFERA chips were mounted on top outside of the vacuum chamber. The top part of the setup with the cold head, the CryoTigers, the turbopump, safety valve and the feedthroughs at the top of the vacuum chamber is shown in figure 54.

For a calibration of the SDDs during a first test run, two X-ray tubes are used. Therefore, two adapters at the front and back of the vacuum chamber allow for the irradiation of the Ti and Zr foils mounted on the sidewalls of the target cell.

To sum up, a schematic drawing showing the entirely assembled SIDDHARTA-2 setup from the top is displayed in figure 55. Here, the electronics on top of the vacuum chamber, as well as the luminosity monitors and outer Veto-1 system (active shielding) and the lead shielding (shown in green) are also included for a better understanding of the final configuration.

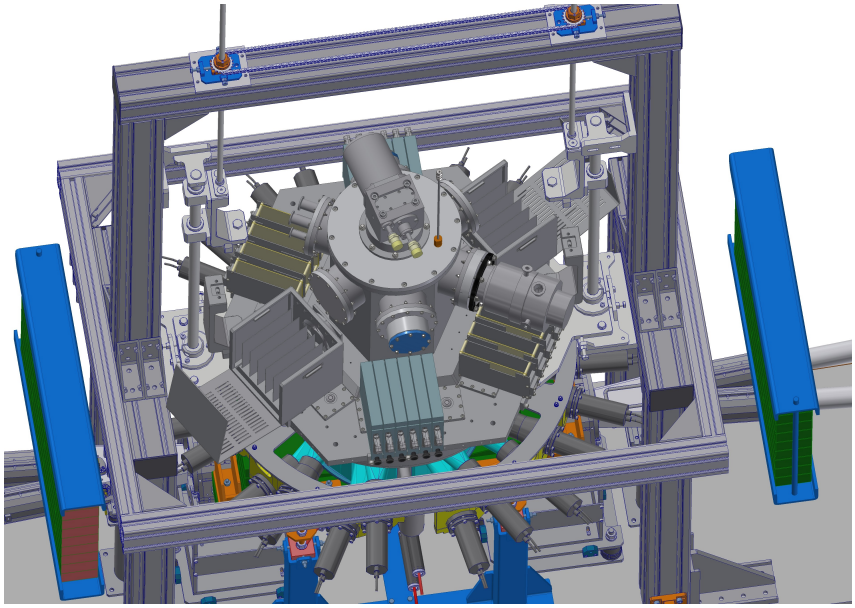

Figure 55: Schematic drawing of a top view of the final SIDDHARTA-2 setup, including the passive and active shielding and the electronics outside of the vacuum chamber. *Picture courtesy of SMI Vienna.*

6.2 Integration of the Veto-2 System

After the initial installation of the general setup as described beforehand, the first veto counters of the Veto-2 system were mounted as well. Five detector boxes corresponding to twenty read-out channels were arranged equidistantly around the target cell. For this, threaded nylon rods were inserted into the bottom aluminium ring of the target cell. Spacers made of polyoxymethylene (POM) were placed onto the rods to ensure a distance between the SDDs and the Veto-2 detectors, needed firstly to protect the sensitive SDDs and secondly to reduce the heat transfer from the veto counters to the SDDs, which have to be operated at lower temperatures than the Veto-2. As a result, another layer of superinsulation was placed between the SDDs and the veto counters as well.
To fixate the veto detectors, nylon washers and nuts were used. The veto counters on the spacers also act as cable routings for the Kapton cables of the SDDs, which are sensitive and cannot be bent too far without causing damage. This configuration is shown in figure 56, where two SDD arrays were mounted on the inside of the aluminium bar on the target cell, and a Veto-2 box was installed directly behind them.

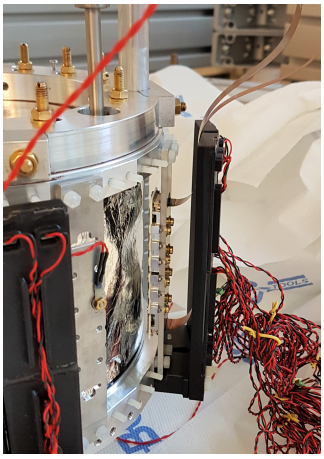

Figure 56: Veto counters of the Veto-2 system mounted behind the SDDs, keeping their Kapton cables in place.

To minimise the space needed inside the vacuum chamber, special cable routings and strain reliefs for the Veto-2 system were mounted in the chamber. During the installation process of the veto counters, it was concluded that a cable length of 125 cm was longer than needed. Therefore, the twisted pair cables from the SiPMs to the feedthroughs were shortened to a length of approximately 70 cm before the final mounting of the detectors, still allowing for a comfortable fixing in the cable routings. To transport the signals from the Veto-2 to the amplification boards, two feedthrough boards, each corresponding to 48 read-out channels, were installed for the veto counters. These connections as well as the strain relief are shown in figure 57.

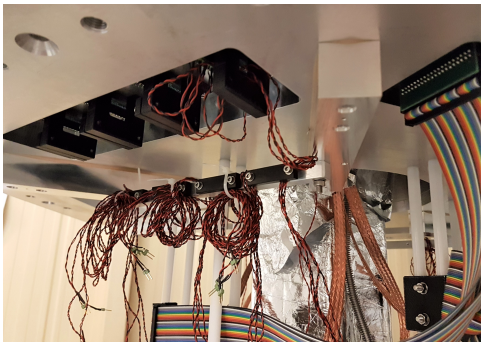

Figure 57: Cable routings and strain reliefs for the Veto-2 system, leading the cables from the SiPMs to the feedthrough boards at the ceiling of the vacuum chamber.

On the other side of the feedthroughs, the twelve-channel amplification boards were mounted. First, they were encased in an aluminium shielding for easier and safer handling and were equipped with small ventilators, to avoid a too high operating temperature during the measurements. Each feedthrough board connects the SiPMs to four amplification boards, one of which can be seen in figures 58(a) and (b), showing the board in its encasement with the ventilator.

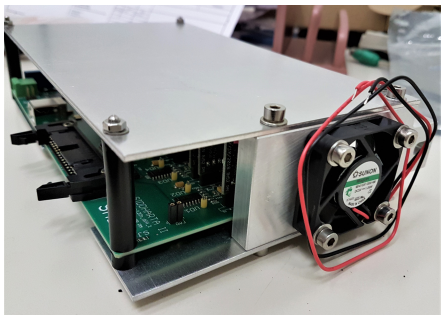

(a) Amplification board for the Veto-2 system in its aluminium encasement with a ventilator for cooling.

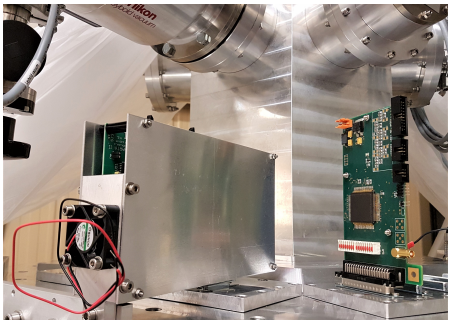

(b) Veto-2 amplification board mounted on a feedthrough board on top of the SIDDHARTA-2 vacuum chamber.

Figure 58: Mounting of the Veto-2 amplification boards.

6.3 Vacuum and Cooling Tests

In December 2018, vacuum and cooling tests were performed. Prior to this, several temperature sensors including silicon diodes as well as PT100 resistors were installed inside the vacuum chamber to monitor the temperature on different locations. For the pumping, a Leybold SCROLLVAC SC 15D forepump together with a Leybold TURBOVAC 350i turbopump were used.
Silicon diode temperature sensors were installed: one on the cold head, one at the top ring of the target cell and one at the bottom ring of the target cell. One PT100 sensor was placed on one CryoTiger, two on the metal frames holding the boards for the Kapton cables of the SDDs, two on the metal bars around the target cell on which the SDDs were mounted, and the last PT100 was installed on one of the Veto-2 boxes, resulting in a total of six PT100 resistors.
After connecting all sensors with their feedthrough parts and closing the setup, the pumping was started. To monitor the temperatures indicated by the silicon diodes, a LakeShore 336 Temperature Controller was used. The resistance of the PT100 sensors was obtained with a digital ohmmeter.
As the vacuum pressure in the chamber reached the 10^{-6} mbar regime, the target cell was filled with 1.44 bar of helium-4 and the cooling was started. The helium compressor (Leybold Coolpak 6000 MD) was switched on to drive the cold head. Although some difficulties with the compressor occurred and its continuous operation was shortly stopped, eventually the problems were resolved and the cooling process was continued. At that point, the target cell was again charged with helium, rising the pressure from approximately 0.13 MPa to 0.14 MPa. This is indicated in figure 59, showing the decrease of the pressure inside the vacuum chamber (figure 59(a)) as well as the evolution of the helium pressure inside the target cell (figure 59(b)), monitored during the cooling process from the moment of starting the cooling.
The error bars in figures 59(a) and (b) correspond to the resolutions of the pressure cells Leybold Center One [36] and GIR/GIA 2000 [37], respectively.

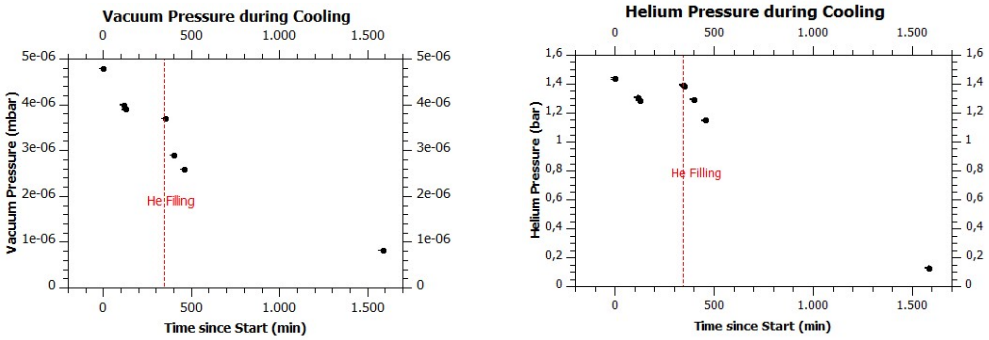

(a) Vacuum pressure over time during the cooling process.

(b) Helium pressure inside the target cell over the course of the cooling process. After approximately six hours, the target cell was refilled with helium (red line).

Figure 59: Pressure curves during the cooling test.

Especially given the large volume of the vacuum chamber and the large surface inside, the eventually reached vacuum pressure in the 10^{-7} mbar range was a satisfying result. Moreover, the pressure in the target cell decreased during the cooling process according to expectations.

The results of the temperature measurements are shown in figure 60(a) and (b) separately for the silicon diodes and the PT100 temperature sensors, respectively. The positions as listed in figure 60(b) are explained in table 3.

	Position in Setup
Pos.1	CryoTiger
Pos.2	Frame for the SDD-electronics
Pos.3	Frame for the SDD-electronics
Pos.4	Metal bar for SDDs on target cell
Pos.5	Metal bar for SDDs on target cell
Pos.6	Veto-2 counter

Table 3: Positions of the PT100 temperature sensors in the setup during the first cooling test.

As figure 60(a) shows, the top ring of the target cell has approximately the same temperature as the cold head after one day of cooling, as would be expected due to the direct connection of them via the cooling line. The bottom ring of the target cell, however, is warmer by approximately 57 K than its top ring. Furthermore, figure 60(b) indicates that the CryoTiger and the metal frames at the top of the target cell have the same temperature of 14°C as well. Since they were not in any direct contact with the cold head or cooling line, and since the CryoTiger was additionally wrapped in superinsulation, they were not cooled down as much as the rest of the monitored locations in the setup.

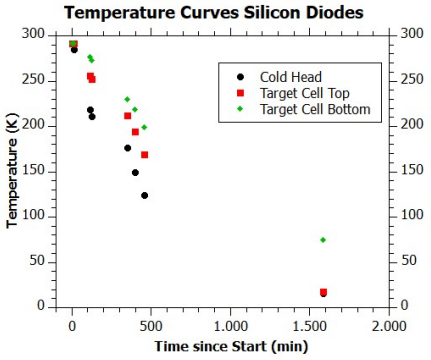

(a) Temperatures measured by the silicon diodes on the cold head and the top and bottom rings of the target cell.

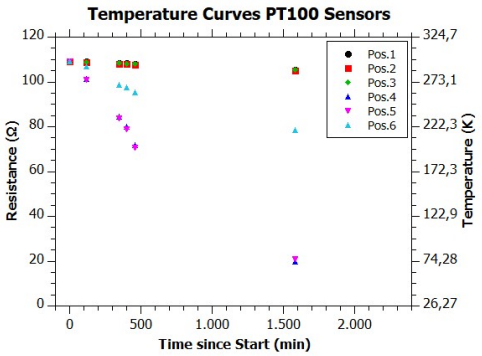

(b) Resistances and temperatures of the PT100 sensors installed on six positions in the setup.

Figure 60: Temperature curves of the silicon diodes and PT100 resistors placed on multiple positions inside the vacuum chamber.

The metal bars on which the SDDs are to be mounted reached temperatures of approximately 76 K. Given the problems with the bonding of the SDDs which occured at temperatures of around 100 K, the bars were cooled down too much and therefore must be better insulated by, for example, using additional nylon washers to further reduce the heat contact from the target cell.
As for the Veto-2 counters, figure 61 shows the temperature curve of the PT100 sensor placed on position 6 on a veto detector box separately.

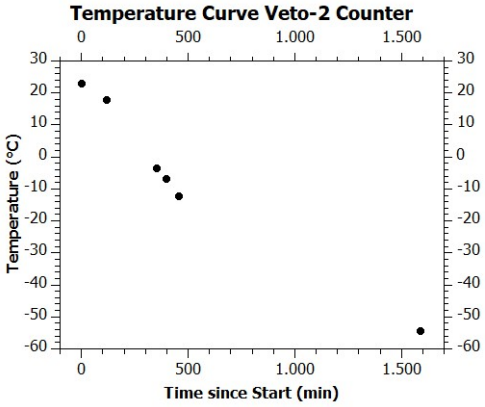

Figure 61: Temperature curve of the PT100 sensor positioned on a Veto-2 detector box during the cooling process.

After approximately one day of cooling, the veto counter reached a temperature of −54°C. As described in chapter 5.5.2, the detectors were tested for temperatures as low as −40°C and their behaviour was found to be temperature-dependent. Since a linear relation between their performance and temperature was indicated, an extrapolation of the results to a temperature of −54°C seems

legitimate. At −40°C, no damage occured to the SiPMs or the scintillators. However, the SiPM datasheet lists a minimum operating temperature of −25°C [31]; the recommended temperature range for the scintillators is even shorter with a minimum of −20°C [32]. Therefore, an increase in temperature of the Veto-2 system could be beneficial to the longevity and reliable operation of the detectors, and could be achieved by adding additional superinsulation between the SDDs and the veto system or minimising the heat transfer by using a new mounting ring with less contact points to the target cell.

7 Conclusion and Outlook

The SIDDHARTA-2 experiment aims to precisely measure the $2p \rightarrow 1s$ X-ray transition in kaonic deuterium to determine the energy shift and width of the ground state with a precision of 30 eV and 75 eV, respectively. This Master's thesis was dedicated to the construction and characterisation of the Veto-2 system for the SIDDHARTA-2 experiment, developed for the suppression of signal-correlated background originating from charged particles. In addition, the Veto-2 is able to act as active shielding to suppress background resulting from kaon stops in the setup by using timing information. The Veto-2 system consists of plastic scintillators with SiPM read-out. After the construction process of the detector units, their performance and properties were studied:

- The crosstalk probability was minimised by determining the optimal shielding configuration between the detector units.
- The time resolution of the Veto-2 system was obtained by the irradiation of the scintillators with a pulsed diode laser and was found to be (293 ± 45) ps, allowing for the application of the veto system as active shielding.
- A detection efficiency of $\sim 99\%$ was determined for the scintillator-SiPM tiles using cosmic rays as probing source.
- At PSI, some of the detector units were damaged in a parasitic pion beam setup. This was confirmed by comparing the I-V-curves of intact SiPMs and SiPMs installed at PSI, leading to the preliminary conclusion that a combination of a high surrounding temperature and high-rate pion flash caused damage to a part of the microcells in the diodes.
- The performance of the detectors as well as the dedicated amplification boards was studied at different temperature points. While the amplification boards were found to operate very stably in a range between 10°C and 40°C, the detector units showed a temperature dependent behaviour. Within the tested range of −40°C to 40°C, the pulse height output as well as the breakdown voltage of the SiPMs varied with the temperature. The observed effects were within expectations. Their evaluation and quantification were crucial for the final electronic configuration in the SIDDHARTA-2 setup.
- Several detector units of the Veto-2 system have already been installed in the SIDDHARTA-2 apparatus at LNF and a first cooling test was performed.

The on-site installation at the beam-line in the DAΦNE accelerator hall will start in February 2019. The beam-commissioning is planned for the beginning

of the same year and a reduced version of the SIDDHARTA-2 experiment, termed SIDDHARTINO, will take data in summer and autumn of 2019, aiming to observe the machine related background at a level similar to that achieved during SIDDHARTA beam time. The kaonic deuterium measurement will take place for several months in 2020.

Abbreviations

ABS	Acrylonitrile Butadiene Styrene
ADC	Analogue-to-Digital-Converter
ASIC	Application Specific Integrated Circuit
CCD	Charge-Coupled Device
CP	Crosstalk Probability
DAC	Digital-to-Analogue Converter
DAΦNE	Double Annular Φ-Factory for Nice Experiments
DAQ	Data Acquisition
DEAR	DAΦNE Exotic Atom Research
EEPROM	Electrically Erasable Programmable Read-Only Memory
FWHM	Full Width Half Maximum
G-APD	Geiger-mode Avalanche Photodiode
GUI	Graphical User Interface
HV	High Voltage
IFES	Intelligent Front end Electronics for Silicon photo detectors
J-PARC	Japan Proton Accelerator Research Complex
KEK	High Energy Accelerator Research Organisation
LDD	Liquid Deuterium Density
LNF	Laboratori Nazionali di Frascati
LV	Low Voltage
LVDS	Low Voltage Differential Signal
MC	Monte Carlo
MIP	Minimum Ionising Particle
NIM	Nuclear Instrumentation Module
PMT	Photomultiplier Tube

POM	Polyoxymethylene
PS	Proton Synchrotron
PSI	Paul Scherrer Institute
QCD	Quantum Chromodynamics
SDD	Silicon Drift Detector
SFERA	SDD Front-End Readout ASIC
SIDDHARTA	Silicon Drift Detectors for Hadronic Atom Research by Timing Application
SiPM	Silicon Photomultiplier
SMI	Stefan Meyer Institute for Subatomic Physics
TDC	Time-to-Digital Converter
ToT	Time over Threshold
USB	Universal Serial Bus
VME/VMEbus	Versa Module Eurocard Bus

List of Figures

List of Tables

References

[1] E. Fermi and E. Teller. The capture of negative mesotrons in matter. *Physical Review*, pages 399–408, 1947.

[2] W. F. Fry. The capture and decay of mesons in photographic emulsions. *Physical Review*, pages 594–597, 1951.

[3] M. Tanabashi et al. (Particle Data Group). *Physical Review D*, page 030001, 2018.

[4] D. Gotta. Precision spectroscopy of light exotic atoms. *Progress in Particle and Nuclear Physics*, page 133–195, 2004.

[5] T. Hyodo and D. Jido. The nature of the $\Lambda(1405)$ resonance in chiral dynamics. *Progress in Particle and Nuclear Physics*, page 55–98, 2012.

[6] Y. Nambu and G. Jona-Lasinio. Dynamical model of elementary particles based on an analogy with superconductivity. i. *Physical Review*, pages 345–358, 1961.

[7] Y. Nambu and G. Jona-Lasinio. Dynamical model of elementary particles based on an analogy with superconductivity. ii. *Physical Review*, pages 246–254, 1961.

[8] J. Goldstone. Field theories with ≪superconductor≫ solutions. *Il Nuovo Cimento (1955-1965)*, pages 154–164, 1961.

[9] Horiuchi, W., Hyodo, T., Weise, W. Kaonic deuterium and low-energy antikaon-nucleon interaction. *arXiv preprint arXiv:1712.09492*, 2017.

[10] S. Deser, M.L. Goldberger, K. Baumann, W. Thirring. Energy level displacements in pi-mesonic atoms. *Physical Review*, pages 774–776, 1954.

[11] DEAR collaboration. Measurement of the Kaonic Hydrogen X-Ray Spectrum. *Physical Review Letters*, page 212302, 2005.

[12] SIDDHARTA collaboration. A new measurement of kaonic hydrogen X-rays. *Physics Letters B*, pages 113–117, 2011.

[13] S. Deser, M.L. Goldberger, K. Baumann, W. Thirring. Observation of Kaonic Hydrogen K_α X Rays. *Physical Review Letters*, page 3067, 1997.

[14] Berucci, C. *Design and Setup of a High Resolution X-ray Detector System to Study Strong Interaction Induced Width and Shift of the 1s Ground State of Kaonic Deuterium.* PhD thesis, University of Vienna, 2017.

[15] T. Mizutani, C. Fayard, B. Saghai, and K. Tsushima. Faddeev-chiral unitary approach to the K^-d scattering length. *Physical Review C*, page 035201, 2013.

[16] N.V. Shevchenko. Near-threshold K^-d scattering and properties of kaonic deuterium. *Nuclear Physics A*, pages 50–61, 2012.

[17] M. Döring and U.G. Meißner. Kaon–nucleon scattering lengths from kaonic deuterium experiments revisited. *Physics Letters B*, pages 663–666, 2011.

[18] A. Gal. On the scattering length of the K^-d system. *International Journal of Modern Physics A*, pages 226–233, 2007.

[19] C. Guaraldo et al. First results on kaonic hydrogen from the DEAR experiment. *The European Physical Journal A - Hadrons and Nuclei*, pages 185–188, 2004.

[20] M. Zobov et al. Test of "Crab-Waist" Collisions at the DAFNE Phi Factory. *Physical Review Letters*, page 174801, 2010.

[21] J. Beringer et al. (Particle Data Group). *Physical Review D*, page 010001, 2012.

[22] M. Iliescu. Precision measurements on kaonic hydrogen and kaonic deuterium: DEAR and SIDDHARTA. *Nuclear Physics A*, page 455c–458c, 2005.

[23] SIDDHARTA collaboration. Kaonic hydrogen X-ray measurement in SIDDHARTA. *Nuclear Phyiscs A*, pages 88–97, 2012.

[24] SIDDHARTA collaboration. First measurement of kaonic helium-3 X-rays. *Physics Letters B*, pages 199–202, 2011.

[25] SIDDHARTA collaboration. Kaonic helium-4 X-ray measurement in SIDDHARTA. *Physics Letters B*, pages 310–314, 2009.

[26] SIDDHARTA collaboration. Preliminary study of kaonic deuterium X-rays by the SIDDHARTA experiment at DAFNE. *Nuclear Physics A*, pages 69–77, 2013.

[27] M. Tüchler et al. A charged particle veto detector for kaonic deuterium measurements at DAFNE. *Journal of Physics: Conference Series*, 2018.

[28] D. Renker. Geiger-mode avalanche photodiodes, history, properties and problems. *Nuclear Instruments and Methods in Physics Research A*, pages 48–56, 2006.

[29] Hamamatsu Photonics K.K. Opto-Semiconductor Handbook Si APD, MPPC. `www.hamamatsu.com/resources/pdf/ssd/e03_handbook_si_apd_mppc.pdf`. Accessed: Jan 14, 2019.

[30] Ketek GmbH. SiPM Working Principle. `www.ketek.net/sipm/technology/working-principle/`. Accessed: Jan 14, 2019.

[31] AdvanSiD. NUV SiPMs Datasheet (Rev.9). `www.advansid.com/products/product-detail/asd-rgb-nuv-4s-p`, 5 2015. Accessed: Feb 13, 2019.

[32] Eljen Technology. General Purpose Plastic Scintillator EJ-200, EJ-204, EJ-208, EJ-212. `www.eljentechnology.com/images/products/data_sheets/EJ-200_EJ-204_EJ-208_EJ-212.pdf`, 1 2016. Accessed: Feb 13, 2019.

[33] C. Sauerzopf et al. Intelligent Front-end Electronics for Silicon photodetectors (IFES). *Nuclear Instruments and Methods in Physics Research A*, pages 113–117, 2011.

[34] M. Cargnelli. Private communication.

[35] CAEN S.p.A. Technical Information Manual (Rev.12). `www.tunl.duke.edu/documents/public/electronics/CAEN/caen_v785.pdf`, 2 2007. Accessed: Feb 13, 2019.

[36] Qerlikon Leybold Vacuum. CENTER ONE Single-Channel Vacuum Gauge Controller Operating Manual GA 09.033/6.02. `www.artisantg.com/info/leybold_centerone_manual.pdf`, 7 2011. Accessed: Feb 13, 2019.

[37] Greisinger Elektronic GmbH. Manual for connection and operation of the GIA 2000 and GIR 2002 (Version 2.8). `www.greisinger.de/files/upload/en/produkte/bda/GIR2002_e.pdf`. Accessed: Feb 13, 2019.